Multi-Domain Modeling of Pan Tilt Platform with Mechanical Imperfections

Author

Muhammad Haider

2009-NUST-MS PhD-Mech-03

Supervisor

Dr Syed Waheed Ul Haq

DEPARTMENT OF MECHANICAL ENGINEERING

COLLEGE OF ELECTRICAL & MECHANICAL ENGINEERING

NATIONAL UNIVERSITY OF SCIENCES AND TECHNOLOGY

ISLAMABAD

August, 2013

Multi-Domain Modeling of Pan Tilt Platform with Mechanical Imperfections

Author

Muhammad Haider

2009-NUST-MS PhD-Mech-03

A thesis submitted in partial fulfillment of the requirements for the degree of

M.Sc. Mechanical Engineering

Thesis Supervisor:

Dr Syed Waheed Ul Haq

Thesis Supervisor

Signature:_____

DEPARTMENT OF MECHANICAL ENGINEERING

COLLEGE OF ELECTRICAL & MECHANICAL ENGINEERING

NATIONAL UNIVERSITY OF SCIENCES AND TECHNOLOGY, ISLAMABAD

August, 2013

Declaration

I hereby declare that I have developed this thesis titled "*Multi-Domain Modeling of Pan Tilt Platform with Mechanical Imperfections*" entirely on the basis of my personal efforts under the sincere guidance of my supervisor Dr. Waheed Ul Haq Syed. All the sources used in this thesis have been cited and the contents of thesis have not been plagiarized. No portion of the work presented in thesis has been submitted in support of any application for any other degree of qualification to this or any other university or institute of learning.

_____

Muhammad Haider

August 2013

Abstract

Pan Tilt Platform (PTP) is a complex electromechanical system whose dynamics is characterized by coupled nonlinear behavior. The system is typically used as mounting platform for surveillance and tracking equipment. Mounted equipment as payload requires accurate position and velocity control from PTP. Velocity control is required in surveillance mode whereas position control is critical in tracking mode. Conventional controller design techniques rely primarily on making more robust controllers by ignoring modeling details of physical system. In demanding applications, it's hard to design controllers for variable operational needs. The problem becomes difficult with the presence of mechanical imperfections in the physical system. These mechanical imperfections include mass imbalance in actuated bodies; friction and backlash at constraint joints of these actuated bodies. Practically, these mechanical imperfections are always present in the physical system since they are difficult to remove.

NUST Man Portable Ground Surveillance Radar System is one such equipment which has Pan Tilt Platform as its mounting and actuating platform. Current study is aimed to model Pan Tilt Platform of the said system. The system requires position control in tilt axis; whereas position and velocity control in pan axis. The study aims at building multiple PTP models having different abstraction levels and fidelity. It starts with a multi-bond graph model of an ideal PTP using Object Oriented Modeling(OOM) approach. OOM approach capture dynamics of individual components of multi-body system and allows system modeling directly from system topology, thereby providing modularity in the model. Ideal PTP model is made more realistic by adding details of actuation mechanisms and mechanical imperfections in step wise manner. At first, a payload as a mechanical imperfection of mass imbalance is introduced as an additional rigid body in tilt axis. Then actuation details of DC servomechanism in pan joint and linear actuator mechanism in tilt joint are added. Finally, mechanical imperfections of

friction and backlash are added in pan joint. Friction is modeled using a general CSVS friction model whereas backlash is modeled using classical dead zone model. Experiments are conducted on PTP of NUST Ground Surveillance Radar to quantify backlash gap and to estimate friction parameters and Inertia. These parameters are estimated using MATLAB Optimization Toolbox. For comparing individual models, their equivalent models are build using MSc ADAMS, Pro/Engineer and MATLAB/Simscape. In the end, pan joint with classical friction and backlash models, is compared with experimental results.

Acknowledgment

In the name of ALLAH, the most Gracious, the most Merciful, who undoubtedly gave me courage to face toughest of the times and gave me hope and strength to accomplish this task.

I am extremely grateful to my supervisor, Dr Waheed Ul Haq Syed for his guidance and motivation throughout my research work. I would also like to acknowledge the efforts of honorable Guidance and Evaluation Committee members Mr Raja Amir Azim, Dr Rizwan Saeed Choudhary and Dr Hassan Saeed Aftab for their help and guidance during this thesis. In particular, I am grateful to Mr Raja Amir Azim for introducing me to bond graph modeling technique and guiding me throughout my study.

I would specially like to mention Ground Surveillance Radar development team for their support during my research work. Special thanks to Dr Mojeeb bin Ihsan for motivating me to select this research topic. Many thanks to Adnan Ashraf and Aamir Javed for their help in conducting experiments.

In the end, I would like to thanks my family in general for their love, confidence and prayers for me and my parents in particular for understanding my passion and support in completion of my studies.

Contents

Nomenclature

LOS Line of Sight

OOM Object Oriented Modeling

PMDC Permanent Magnet Direct Current

PTP Pan Tilt Platform

v average interface velocity

z average bristle deflection/displacement

α Half of backlash gap

$\dot{\theta}_p$ Euler rate pan

$\dot{\theta}_t$ Euler rate tilt

γ Stribeck tuning parameter

μ Coefficient of friction

ω angular velocity

σ_0 average bristle stiffness

σ_1 bristle damping

τ Torque

θ_d displacement in backlash gap

θ_l load angular displacement

θ_m motor angular displacement

d_m mean diameter of lead screw

F Force

F_c Coulomb Friction

F_e External Applied Force

F_f Friction Force

f_n Normal Force

F_s Stiction/Static Force

F_v Viscous Force

h angular momentum

J_l load inertia

J_m motor inertia

K_t motor torque constant

L_e Coil Inductance

p linear moment of rigid body

R_z Rotation Matrix about Z-axis

R_e Coil Resistance

t_d Dwell time

t_s Slip time

v_s Stribeck Coefficient

c viscous damping

f coefficient of friction between screw and nut

i motor current

k Stiffness

l lead of the screw

N gear ratio

T Shaft Torque

u motor input signal

List of Figures

List of Tables

Chapter 1

Introduction

1.1 Pan Tilt Platform

Pan-tilt platform is a mechanism assembly that provides two D.O.F in pan and tilt axis. It can be considered as a two-axis gimbal assembly with independent actuating mechanisms. It finds its application as mounting and actuating platform for surveillance and tracking equipment. The current study is part of development of Pan Tilt Platform for NUST Ground Surveillance Radar[1] shown in Figure 1.1.

Figure 1.1: NUST Ground Surveillance Radar

[1]NUST Ground Surveillance Radar is being developed by Microwave Engineering Research Lab (MERL), College of Electrical and Mechanical Engineering, NUST.

Figure 1.2 shows Pan Tilt Platform of NUST Ground Surveillance Radar in a close view, with description of its pan and tilt motion about their respective motion axis.

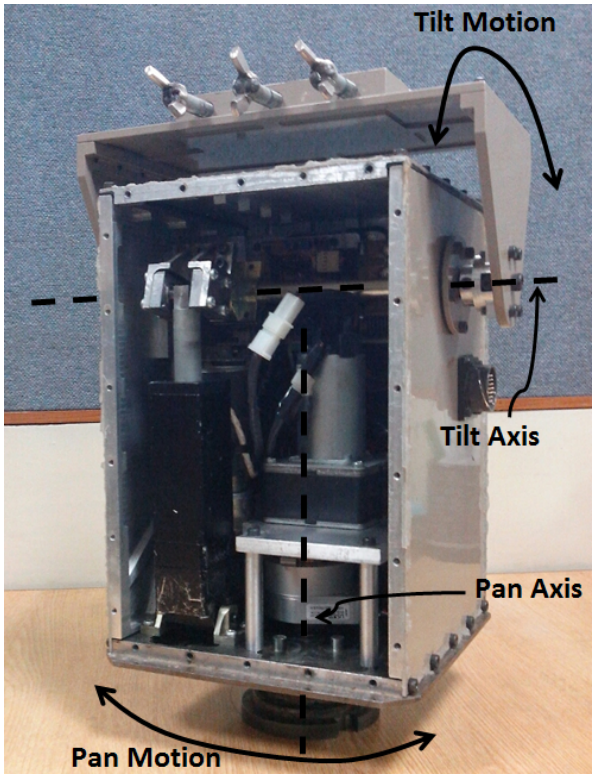

Figure 1.2: Pan Tilt Platform of NUST Ground Surveillance Radar

1.2 Problem statement

Performance requirements for PTP is defined by the operational requirements of the payload. For given system, operational requirements of the payload demand position control in tilt axis; whereas position and velocity control in the pan axis. Position control in tilt axis is not stringent and is primarily used to make Radar to see in the desired Line of Sight(LOS). Position control is in open loop configuration which requires operator input to set tilt position best suitable for Radar operations. In pan axis, for implementing position and velocity control a closed loop control strategy is implemented by using a servo-mechanism. Pan axis has two distinct modes of operation; surveillance and tracking mode. In surveillance mode, controller task is to maintain constant velocity whereas in tracking mode the goal of controller is to actuate system to the required position. System shows different dynamics for these operational goals since the system

has a nonlinear behavior. It becomes difficult to adjust gains for linear controllers for such non-linear systems.

Non-linearity in Pan Tilt Platform dynamics arises from different sources. Pan Tilt Platform is a typical multi-body systems whose dynamics is governed by non-linear dynamic equations [1]. Non-linearity also arises in system dynamics because of mechanical imperfections in the physical system. These imperfections are present in rigid bodies and at their inter-connecting joints. Rigid body can have imperfection of mass distribution; typically mass imbalance in actuated axis. Irregularity in mass distribution can greatly affect dynamics of the system. PTP can be considered as different case studies for different mass distributions. In given case, PTP carries payload and therefore its in an unbalanced configuration. This configuration causes system to exhibit non-linear and coupled behavior. Coupling causes change in system parameter of pan axis due to change in tilt position. Mass imbalance also introduces non-linearity in tilt dynamics since gravity effects appears in system dynamics. Mechanical imperfections at joints; friction and backlash, also introduces hard non-linearity in the system due to their intrinsic nature [2]. These imperfections are always present in a realistic joint since their removal from the system is not a cost effective solution.

It is more practical to tackle these non-linearities in controller design. One of the approaches in controller design for such applications demand detailed modeling of the physical system. By doing so, dynamics of the physical system is captured by a mathematical model which can be further analyzed using mathematical tools. The current problem at hand is to build a multi-domain model of PTP with mechanical imperfections of mass imbalance, friction and backlash.

1.3 Motivation

Motivation for the study of Pan Tilt Platform comes from the improvements required in the PTP of NUST Ground Surveillance Radar NRv3 shown in Figure 1.1. Effects of mechanical imperfections are pronounced in the present version of PTP. High mass imbalance in tilt axis makes it a highly coupled system which changes system parameters in pan axis. Moreover, friction and backlash in pan axis makes dynamics non-linear. Linear PID Controller gains are adjusted using conventional methodologies that rely on

a hit and trial experimental approach. The implemented control strategy shows limitation in operations.

This study is initiated to better understand mechanical imperfections and their role in system dynamics. The understanding can be used in future design improvements of PTP. Moreover, a detailed PTP model, the outcome of the study can be used in future controller design studies.

1.4 Objectives

The study has been conducted with the following objectives in mind.

1. Multi-bond graph modeling of Ideal Pan Tilt Platform(PTP) using Object Oriented Modeling
2. Addition of payload to ideal PTP and modeling details of multi-domain actuation mechanism
3. Addition of mechanical imperfections (joint friction and actuator backlash) in PTP

1.5 Modeling Methodology

The study is aimed to model PTP with mechanical imperfections. PTP is multi-domain system and Bond Graphs modeling is considered a useful tool in study of such systems [3]. Further, the objectives clearly states that the modeling details are to be added in step wise manner. Therefore, Bond Graph modeling is utilized with Object Oriented Modeling approach to model multi-body dynamics. Later, Bond Graph models of PMDC geared motor with controller details are added to pan joint. Similarly, Bond Graph model of Linear Actuator with its tilt mechanism are added in Tilt joint. In the end, a general classical friction model of CSVS along with classical backlash dead-zone model is used to model mechanical imperfection in pan joint.

1.6 Literature Review

Different attempts have been made to model PTP or two-axis gimbals assembly in literature [3–7]. It has been reported that bond graph modeling is considered a useful tool

for modeling multi-domain systems as it gives clear insight to the power exchanges between different components of the system which is not evident in classical formulations [3]. In one of the modeling attempts, a Newton-Euler scalar bond graph model of three axis gimbal assembly was build which is a generalized PTP case [4]. The BG model was compared with its Lagrangian equivalent. The study claims that BG model was computationally more efficient than its comparative model. In another study, PTP was modeled using scalar bond graph technique with controller design perspective [5]. The system was considered as an uncoupled system since it was assumed that mass distribution is in completely symmetric and balanced configuration. In another study, a scalar bond graph model based on Lagrangian formulation was built [6] The study showed that coupling exists in partially symmetric system even if the system has balanced mass distribution. Such coupling effects are pronounced at much higher speeds than what are practically encountered [8].

For representing 3D multi-body systems in an efficient way, multi-bond graph technique was proposed [9]. Bond graph representation typically requires derivation of system equations in first place using classical formulations. Moreover, it becomes difficult to retain the topological information of the complex multi-body systems. The representation is also not suitable for extensibility of models. In attempt for making bond graph models more efficient, attention was given to combine object oriented modeling approach with bond graph technique [10, 11]. The approach focus on capturing the dynamics of an individual component of the domain. Their dynamics are given by classical formulations to build encapsulated or wrapping models. System model can be build by joining these encapsulated models using topological information of the physical system. Combination of OOM approach with bond graphs, allow derivation of system equations using algorithmic nature of bond graphs [11]. The step can be carried out using commercial software like 20-sim. Object oriented modeling also supports modular approach for re-usability and extensibility of model [12]. Therefore, combining of multi-bond graph technique with object oriented modeling is a natural choice for modeling 3D multi-body systems.

In an attempt, a PTP model as camera platform was build in DYMOLA environment using scalar bond graphs and object oriented modeling approach [7]. Recently, a multi-bond graph library of 3D multi-body components is proposed based on OOM

approach using 20-Sim [13]. These components include rigid body and their interconnecting joints (spherical, rotational and translational joints). Rigid body is modeled using Newton-Euler formulation and joints are modeled by their respective transformations. The advantage of using OOM approach with multi-bond graph is to build the model directly from the system topology.

Friction, is the resistive force that appears when relative motion exists between two sliding surfaces in contact [2, 14, 15]. Friction plays vital role in some of our everyday life actions like one can walk or run on the surface because of friction at the contact patch. Similarly cars can roll over the road, they can steer at the corner turns and most importantly their braking is possible due to friction [15]. But in certain applications, friction role is undesirable [16] and because of practical reasons it can't be eliminated from the physical system. Friction in mechanical systems like Pan Tilt Platform where accurate position and velocity control is required, can deteriorate the system performance. The performance is degraded by appearance of steady state errors, limit cycling and hunting in the system [17–19]. The problem can be tackled if friction is predicted using models and then its effects can be compensated in the controller design [20]. In literature [15, 21–25], friction prediction is done by using mathematical models that can reproduce different friction phenomenon. Friction exhibits different phenomenon which makes it an interesting problem to model and study.

These models can be divided into two categories; classic and dynamic models [2]. Classical or static friction models don't introduce any state variable in system dynamics and can predict friction with any combination of Coulomb, Static, Viscous and Stribeck friction parameters using system state [25]. On the other hand, dynamic models introduce state variables in the system dynamics. These models are capable of capturing complex dynamic behaviors like pre-sliding displacements, stick-slip motion, frictional lag and varying breakaway torque. These include Dahl, LuGre and Leuven models [2]. Brief description of static friction models and LuGre friction model is given in next chapter. Initially, it was planned to use LuGre friction model in PTP model, since it captures more friction phenomenon than classical models and is one of the widely used dynamic model for modern controls applications [26]. During dynamic parameters estimation of LuGre friction model from experimental data, it was concluded that the feedback encoder resolution is far less than what should be needed to capture pre-

sliding displacement at the joint. As a result, PTP is modeled with classical CSVS frictional model which predicts friction using Static, Coulomb, Viscous, and Stribeck friction parameters.

Backlash, in mechanical system is generally referred to the presence of free play between adjacent moveable components [2, 27, 28]. This typically arises because of the tolerances in designing and manufacturing of different mechanism components essential to achieve desired relative motion. This phenomenon is common in mechanical systems with power drives and gearboxes. Presence of backlash, can affect the performance of systems like Pan Tilt Platform under closed loop velocity and position control [29]. Backlash switch the system between two distinct modes: contact and free dynamics mode [30]. The switching of modes introduces highly changing torque generation and distribution. This changing behavior makes control difficult as oscillatory behavior appears in the system. In some cases, backlash may cause limit cycles as well [27].

For practical reasons, backlash is difficult to be removed from physical system. But backlash in these systems can be tackled by predicting and compensating its non-linearity and improving the capability of linear controllers [31]. Backlash is modeled by different mathematical models described in literature. These are dead-zone, hysteresis and impact based models [18, 27, 29]. Dead-zone and hysteresis are generally referred as classical backlash models [29]. These are relatively simpler non-linear models that uses system state variables to switch system modes and dynamics. Both dead-zone and hysteresis models assume inertia less shafts and plastic collision at the interface. Dead-zone assumes flexible shafts with negligible internal damping whereas hysteresis model assumes rigid shafts [29]. On the other hand, Impact based dynamic models capture the transition of backlash to contact mode while considering elastic collision at the contact interface [18]. This introduces additional state variable but the model outperforms classical models when predicting dynamics at low amplitude motions which are predominated by stable impact patterns [32]. A brief description of classical models for backlash are given in next chapter. In PTP model, backlash is modeled using dead-zone classical model. The model is one of the widely used models in literature [29]. It is also selected since it's required parameter of backlash gap is feasible to be quantified.

1.7 Thesis Outline

Keeping in view objectives of research, the study is presented in following layout.

Chapter 1 (Introduction) introduces the research study by discussing problem statement, objectives and the modeling methodologies.

Chapter 2 (Modeling Methodology) presents brief literature review of the topic followed by explanation of different physical phenomenon and their modeling methodologies. It discusses multi-body dynamics using object oriented modeling. Briefly explains friction and its observed behavior along with backlash and its classical models.

Chapter 3 (System Modeling) builds Pan Tilt Platform models having different abstraction levels and fidelity using methodologies discussed in chapter 2.

Chapter 4 (Parameters Estimation) discusses the experiments and parameter estimation procedures for backlash and friction models.

Chapter 5 (Results) presents results and simulations of different PTP models introduced in Chapter 3.

Chapter 6 (Conclusion) concludes the research work with the little description of work that can be conducted in future.

Chapter 2

Modeling Methodology

.

2.1 Bond Graphs

Bond graph is a powerful graphical tool for representing power exchange phenomenon in physical system [33–35]. The technique is useful to study power exchanges involving different physical domains [36]. These domains are considered as subsystems exchanging power with the help of interconnecting points. Subsystems are further represented as generic power exchange elements connected together to represent the dynamics of the subsystem [1]. A brief introduction for better understanding of bond graph modeling of physical system is presented here.

2.1.1 Ports, Bonds and Power variables

Power exchange takes place between different domains at their inter-connecting points. These points are known as ports. A port that can exchange power is known as power port. Sometimes, data or information is also shared between different domains. Ports that has negligible amount of power sharing but allow data exchange are known as signal/control ports [1].

Power or data exchange between different components or elements is represented by the use of arrows. Power exchanges is being represented by half arrows whereas, signal transfer is being represented by full arrows [37]. Figure 2.1 shows power and control bonds in a bond graph model of PMDC geared motor. Power arrow is also termed as

bond lines or simply bonds. A bond joins a power outflow port from one component to a power inflow port of another component. Direction of arrow/bond shows the assumed power flow direction. Similarly, lines connecting control output ports to control input ports are termed as control bonds [1].

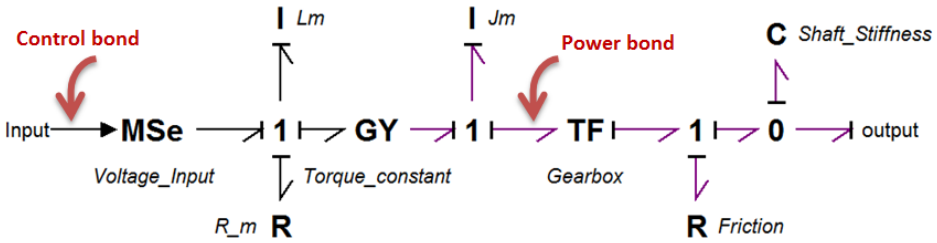

Figure 2.1: Power and Control Bonds shown in Bond Graph model of PMDC motor

In physical system, power or information exchange between components is a complex phenomenon. However, power exchange phenomenon at power ports can be described by product of power variables, the effort and the flow variables. The bond is considered to conserve the magnitudes of flow and effort variables at both ends. In a bond, the directions of effort and flows are opposite. Direction of effort is being represented by placing a small vertical line, the causal stroke. Causal stroke is placed at the port that receives the effort variable. The same port acts as output port for flow variable. Similarly, control bond delivers signal while conserving its magnitude [1].

Power variables are different in different physical domains. In mechanical domain, force and torque are effort variables whereas velocity and angular velocity are flow variables. In electrical domain voltage is an effort and current is a flow variables. These variables are listed in Table 2.1

Table 2.1: Power variables of different physical domains [1]

Domain	Effort variable	Flow variable
Mechanical (Translation)	Force	Velocity
Mechanical (Rotational)	Torque	Omega
Electrical	Voltage	Current

Bonds represent scalar power quantity. Single bond is typically used for representing power exchange between two ports. The bond graphs with single bond is also termed as Scalar Bond Graphs. For 3D multi-body systems, scalar bond graphs are

not an efficient modeling tool. Multi-bond graphs were proposed and were suitable for handling such systems [38]. Multi bonds are represented by double line half arrows. They are sometimes also known as vector bond graphs; however multi-bonds do not represent any vector. They only represent 3D scalar power variables in column matrix. Direction of effort / flow in a bond is shown by a causal stroke. Causal stroke is a short, perpendicular line drawn at one end of the bond, indicating the direction of effort variable.

2.1.2 Elementary Components

Physical processes in different domains can be explained by combining different generic elementary components. These components are presented here

2.1.2.1 1-port Elements

Power exchange takes place in some elements via single port. They can be energy source, storage or dissipative elements [1].

Energy Source Elements

These elements are sources of power variables in the system.

Source of Effort, represented by Se (in modulated form by MSe). Force, torque and voltage are effort sources in mechanical translation, rotational and electrical domain.

Source of Flow, represented by Sf (in modulated form by MSf). Velocity, angular velocity and current are sources of flow in mechanical translation, rotational and electrical domain.

Energy Storage Elements

These elements have the ability to store incoming energy either in the form of kinetic or potential energy. Their intrinsic nature dictates what kind of energy they can store. Causality explains whether an energy storage element get its preferred form of energy as input or not? If storage element is in preferred state, it is in integral causality, whereas if it's not in preferred state, it is in differential causality. Number of energy storage

elements in integral causality, dictates number of state variables of the system. These energy elements are;

Inertial elements, represented by I, and are effort integrators. They prefer effort as input variable. In integrally causaled state, their output is generalized momentum, a state variable. Inertial element in mechanical translation domain is mass; moment of inertia in mechanical rotational domain; inductance in electric domain.

Compliance elements, represented by C, and are flow integrators. They prefer flow as input variable. In integrally causaled state, their output is generalized displacement, a state variable. Springs and capacitors are compliance elements in mechanical(rotational/translational) domain and electrical domain respectively.

Energy Dissipative Element

Resistor elements, represented by R, is a power dissipator and relates flow and effort variables. Damper and electric resistor are resistor element in mechanical and electrical domain respectively.

2.1.2.2 2-port Elements

These elements explain power transfer using two ports. These are power conserving elements.

Transformers represented by TF (in modulated form MTF). They have multiplying effect for incoming effort and flows. Transformer modulus relates flows and efforts of the two ports. Gears and electric power transformers are transformers in mechanical and electrical domain. In mechanics, transformers also represent geometric transformations and kinematic relationships.

Gyrators are represented by GY (in modulated form MGY). They convert the nature of power variables i.e. incoming flow is converted into outgoing effort and vice versa. Gyrator modulus relates flows and efforts of the two ports. Gyroscope and motor are gyrators.

2.1.2.3 3-port Elements

Three port elements are also power conserving elements. They are primarily used to inter-connect other subsystems and basic elements.

0-junction element, represented by "0". It is same effort and a flow summer junction.

1-junction element, represented by "1". It is same flow and effort summer junction.

2.2 Multi-Body Dynamics - An OOM approach

Modern applications demand critical analysis of physical systems which requires detailed modeling often involving multi-domain dynamics. One of the approaches to cope with the complexities involved in detailed modeling of physical systems is to build them using hierarchical approach by building library of reusable basic components of single domain as sub-models [38]. Object Oriented Modeling(OOM) approach whose concept is more familiar in computer sciences where it helps in better organizing large computer programs by providing data exchange interfaces between small reusable computer codes. Soon it was realized that the same approach can be used for modeling complex physical systems [38]. In one such attempt, a library was build in 20-Sim environment for Multi-body system components using object oriented modeling approach [13]. Reusable sub-models are build by defining dynamics of individual components which allows data exchange through its interface ports. The study [13] considered two components of multi-body system; rigid bodies and their inter connections (joints of different types). These sub-models are represented in encapsulated form similar to word bond graphs, but this representation is different from word bond graphs as OOM representation is capable of deriving complete system equations using algorithmic nature of bond graphs [8].

2.2.1 Rigid Body

A simple rigid body can be represented as shown in Figure 2.2 where marker (reference coordinates) at center of gravity is placed such that x, y and z axes are aligned with body principal axes.

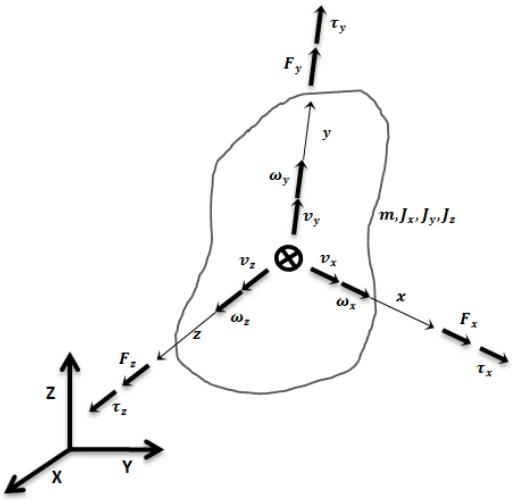

Figure 2.2: Rigid Body representation [8]

Rigid body dynamics can be captured by Newton-Euler formulation given by [13]

$$F = \frac{\partial p}{\partial t}\,|_{rel} + \omega \times p \tag{2.1}$$

$$\tau = \frac{\partial h}{\partial t}\,|_{rel} + \omega \times h \tag{2.2}$$

where F, the force applied at the c.g, τ, the torque applied about principal body axes, p, the linear momentum of rigid body, ω, the angular velocity about principal body axes, h, angular momentum about the principal body axes

Based on OOM approach, dynamics of rigid body given by Equations 2.1 & 2.2 can be represented using multi-bond graphs. This representation is shown in Figure 2.3 along with gravity as an external force. The model gives flows and efforts at the center of gravity of rigid body.

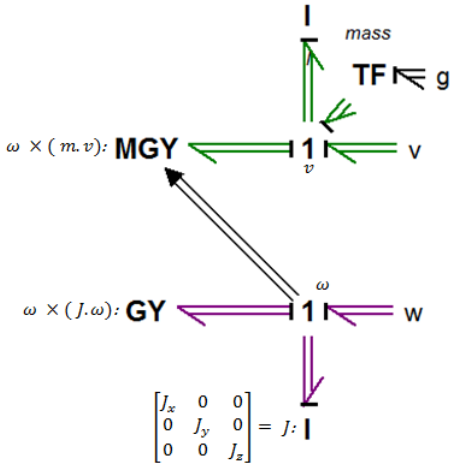

Figure 2.3: MBG model of rigid body with gravity using OOM approach [8]

2.2.2 Revolute Joint

Joint dynamics can be explained by using simple transformations defining constraints it is offering. A simple revolute joint between two rigid bodies is shown in Figure 2.4. A revolute joint has single degree of freedom and its dynamics can be explained by following transformations [13]

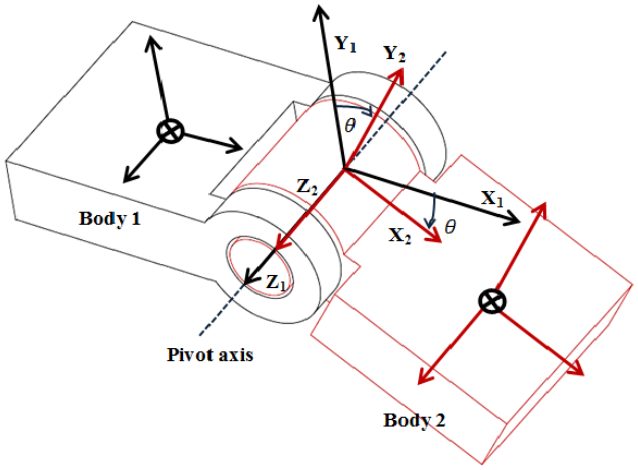

Figure 2.4: A simple revolute joint between two rigid bodies [8]

$$\begin{Bmatrix} v_{x1} \\ v_{y1} \\ v_{z1} \end{Bmatrix} = R_z \begin{Bmatrix} v_{x2} \\ v_{y2} \\ v_{z2} \end{Bmatrix}; \begin{Bmatrix} F_{x2} \\ F_{y2} \\ F_{z2} \end{Bmatrix} = (R_z)^t \begin{Bmatrix} F_{x1} \\ F_{y1} \\ F_{z1} \end{Bmatrix} \tag{2.3}$$

$$\begin{Bmatrix} \omega_{x1} \\ \omega_{y1} \\ \omega_{z1} \end{Bmatrix} = R_z \begin{Bmatrix} \omega_{x2} \\ \omega_{y2} \\ \omega_{z2} \end{Bmatrix}; \begin{Bmatrix} \tau_{x2} \\ \tau_{y2} \\ \tau_{z2} \end{Bmatrix} = (R_z)^t \begin{Bmatrix} \tau_{x1} \\ \tau_{y1} \\ \tau_{z1} \end{Bmatrix} \tag{2.4}$$

where

$R_z = \begin{bmatrix} c_\theta & -s_\theta & 0 \\ s_\theta & c_\theta & 0 \\ 0 & 0 & 1 \end{bmatrix}$ is the rotation matrix

Joint markers 1 and 2 are attached to body 1 and 2 respectively. Using OOM, revolute joint dynamics can be represented with bond graphs as shown in Figure 2.5.

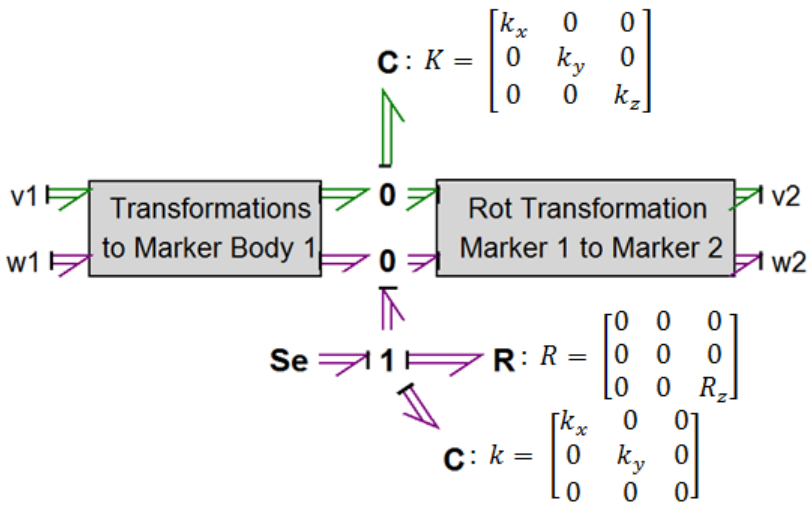

Figure 2.5: MBG model of revolute joint using OOM [8]

Another important transformation is between joint marker and marker at center of gravity of rigid body. Mass center markers of both bodies are shown in Figure 2.4. The dynamics is explained by following relationships

$$\begin{aligned} \tau &= r \times F \\ v &= \omega \times r \end{aligned} \tag{2.5}$$

where, r represent position vector of joint marker from body mass center marker. MBG model of this transformation is shown in Figure 2.6 using object oriented modeling approach.

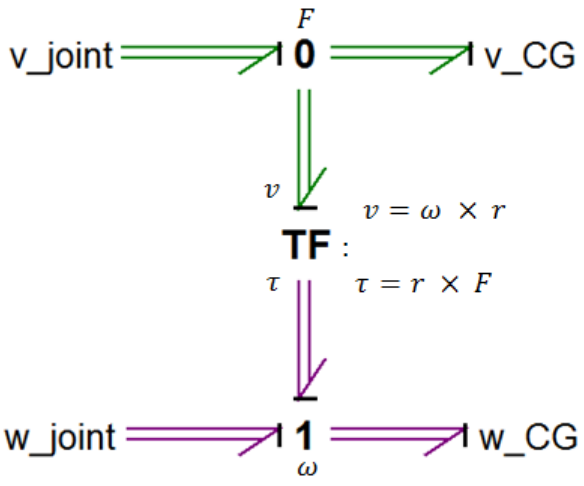

Figure 2.6: Linear transformation between markers [8]

2.3 Mechanical Imperfections

Imperfections are complex phenomenon in physical system that are generally ignored while modeling ideal physical system. State of physical irregularities depends on imperfections in individual bodies and in their inter-connections i.e. joints.

2.3.1 Body Imperfection

2.3.1.1 Mass Distribution

It gives description of how regularly mass is distributed within the rotating body w.r.t pivot axes. Mass distribution can be better explained using following two terminologies.

Symmetry explains how body principal axes are aligned with the pivot axes. If none of the axes are aligned, the system is in unsymmetrical configuration, whereas if one of the principal axis is aligned with pivot axis then assembly could be in completely or partially symmetric configuration depending on whether moment of inertia about non-rotating principal axes are equal or not [4].

Balancing explains the position of center of gravity w.r.t pivot axes. If body C.G lie on the pivot axis, the assembly is in balanced configuration otherwise it's in imbalance configuration.

Table 2.2: System Behavior dependency on Mass Distribution Configuration

Configuration		System Behavior	
Symmetry	Balancing	Linearity	Coupling
Completely Symmetric	Balance	Non-linear	Un-coupled
Partially Symmetric	Balance	Non-linear	Coupling effect at higher speeds
Symmetric	Imbalance	Non-linear	Coupled
Asymmetric	Balanced	Non-linear	Coupling effect at higher speeds
Asymmetric	Imbalance	Non-linear	Coupled

Table 2.2 summarizes the role of mass distribution on system dynamics. It can be seen that system has non-linear behavior in all mass distribution configurations due to 3D motion. However, coupling in system dynamics is dependent on the mass distribution configuration. For completely symmetric and balanced configuration, system

has an uncoupled behavior. For balanced and partially/asymmetric configuration, practically system can be treated as an uncoupled system since coupling arises at higher speeds. But for an imbalanced configuration, system dynamics shows coupling due to appearance of gravity in system dynamics.

2.3.2 Joint Imperfection

Joints provide desired relative motion between two bodies with pre-defined constraints. Joints for their working, introduce few imperfections in the system. These imperfections are:

2.3.2.1 Friction

Friction is a complex nonlinear phenomenon, which arises at the contact interface of two adjoining surfaces under relative motion due to applied external force [2, 14, 15]. Wide range of physical phenomena are regarded as the cause of friction. This includes elastic and plastic deformations, fluid mechanics, wave phenomena and material sciences [39]. Historically friction is being studied in classical mechanics but lately there has been a strong resurgence in friction due to demanding engineering applications [39]; control engineering is one of these areas. Recent studies have been possible because of availability of new precise measurement techniques.

In classical mechanics, friction study dates back to Leonardo da Vinci, Guilliame Amonton and Charles de Coulomb [40]. Amonton concluded about friction that it is proportional to normal force but counter-intuitively is independent of the apparent contact surface area. His conclusion is also referred in text as Amonton's paradox. Later on, this paradox was solved by the development of appreciation for the difference in true contact area and apparent contact area. Because of irregularities at the contact surfaces, true contact between the surfaces is very small as compared to the apparant contact area. By increasing normal force, in reality the true contact area increases, which ultimately increases the friction force [40]. Similarly, Coulomb found that friction has magnitude proportional to normal load but is opposite to direction of motion. In early 20th century, Stribeck found that friction has dependence on the velocity as well. The phenomenon that is known as stribeck effect today [40].

With the advent of precise control applications, where low speed, high reversal velocities and accurate position controls are required, friction role in these systems asked for more rigorous studies. Friction behavior was studied for different velocity regimes and based on experimental data, more comprehensive dynamic models were presented that tries to capture most of the physical behaviors that friction exhibit. Before, introducing different friction models, it will be appropriate to explicate different friction phenomenon that are experimentally observed.

2.3.2.1.1 Friction phenomenon Friction can be best explained by considering it as a phenomenon whose dynamics are represented by two distinct modes. First is the stiction and the other is sliding mode. In stiction mode, external force is not large enough than friction force and therefore there is no slippage at the contact interface, whereas in sliding mode, external force overcomes the frictional force and slippage occurs at the interface.

2.3.2.1.1.1 Varying Break-Away Friction The force that is required to overcome stiction and induce a slippage at the contact interface is termed as break-away friction. Experimental results have shown that break-away friction is not a consistent phenomenon. In literature [41], it has been suggested that this behavior depends on the dwell-time while sticking and the rate of increase of the applied force. A typical dependency of break away torque on varying rate of applied force is shown in Figure 2.7.

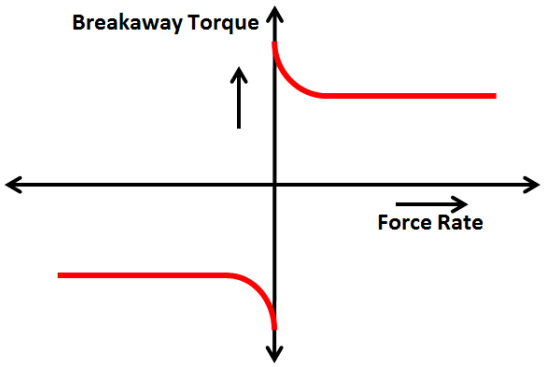

Figure 2.7: Varying breakaway force as function of force rate

2.3.2.1.1.2 Stribeck Effect Experimental results conducted by Stribeck suggested that friction force is also a function of velocity. The effect is more pronounced when sliding starts between two surfaces. The phenomenon can be explained by dividing it in four distinct regimes [23]. These regimes and their physical representation is shown in Figure 2.8. The first regime is the stiction, where asperities at both surfaces deform elastically. There is no slippage during this regime. In second regime, slippage occurs but the interface velocity is so low that development of consistent lubrication film is not possible. The regime is also termed as boundary lubrication. Regime 1 and 2 are considered solid to solid friction regimes. In third regime, velocity is developed to a level where partial lubrication is possible. Solid to solid friction is still possible. Typically, stick-slip phenomenon occurs in this regime. In forth regime, the velocity is developed to a level where the thickness of lubrication layer becomes greater than the height of contact asperities. The friction force is dominantly a viscous effect in this regime.

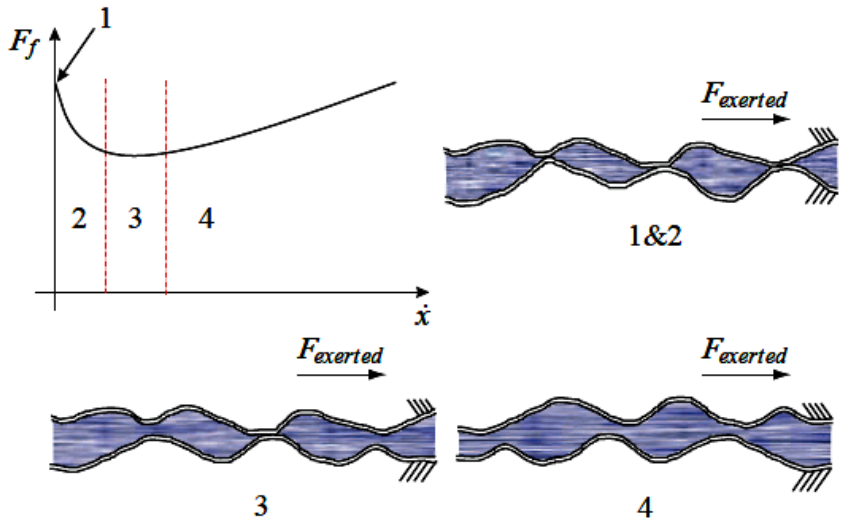

Figure 2.8: Stribeck friction curve divided into four regimes [23]

2.3.2.1.1.3 Pre-sliding Displacement In stiction mode, where external force is less than breakaway force, friction acts like a spring force [41]. The behavior arises due to effective stiffness of contact asperities. The displacement is at micro-level and no slippage occurs at macro level. This phenomenon influences when studying systems with velocity reversals.

Pre-sliding displacement can be divided into elastic and plastic deformations. Because of plastic deformation, a hysteresis loop is observed in pre-sliding regime. The

behavior is shown in Figure 2.9, where friction force is a function of pre-sliding displacement.

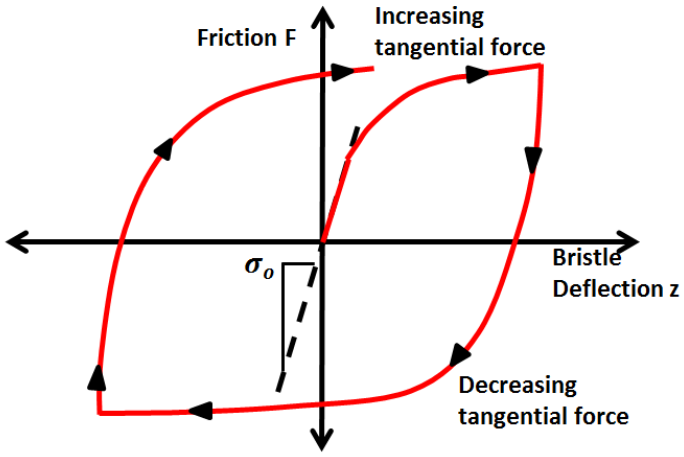

Figure 2.9: Friction force as function of pre-sliding displacement

2.3.2.1.1.4 Stick-Slip Motion This phenomenon is typically observed in low velocities or at near zero velocities, where external force is varied in order to attain a constant velocity at the interface. The phenomenon is observed as a sudden jerking motion. Friction is being switched between stiction to slippage mode or vice versa. During stiction, external force has to be greater than static friction force in order to initiate any motion. As soon as motion is initiated friction force is decreased suddenly due to stribeck effect. This causes an overshoot in velocity than the required speed. In order to lower the attained velocity to desired level, external force is decreased but now it becomes less than static friction force and the system switches back to stiction mode. The whole cycle is repeated again. The behavior is shown in Figure 2.10

It can be seen that the velocity keeps on changing from zero to some small non-zero number. The time the interface is at rest is referred as the dwell time and is shown as t_d, whereas the time for which the interface is in motion is termed as slip time and is denoted by t_s.

Stick-slip motion induces limit cycles in servo-mechanisms and can greatly affect the system performance.

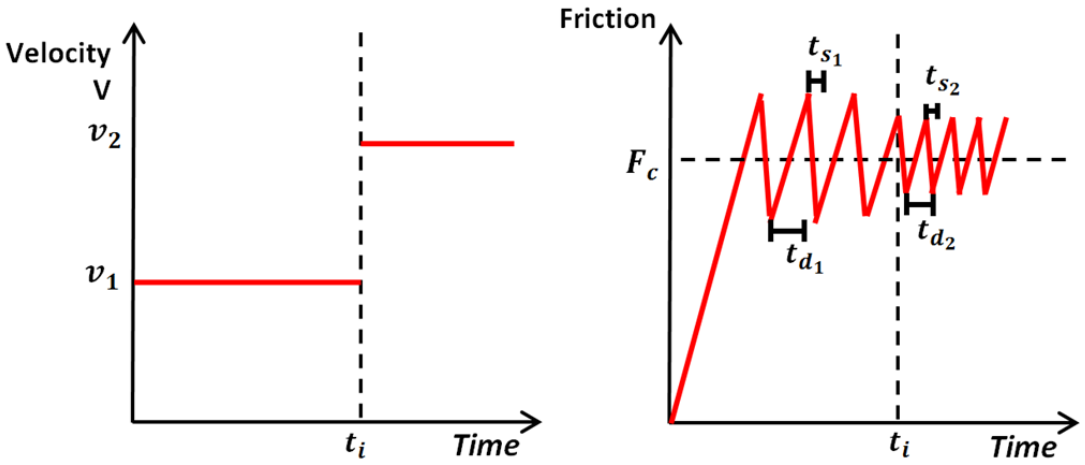

Figure 2.10: Stick-slip motion

2.3.2.1.1.5 Frictional Lag Frictional lag is the delay in the change of the friction force as function of a change in the velocity. Friction force and velocity relationship shows hysteresis behavior i.e; the friction force is less when velocities at interface is decreasing whereas an increased in frictional force is observed when the velocities are increasing. The width of the hysteresis loop increases with frequency and with higher rates of velocity changes. Typical hysteresis behavior is shown in Figure 2.11.

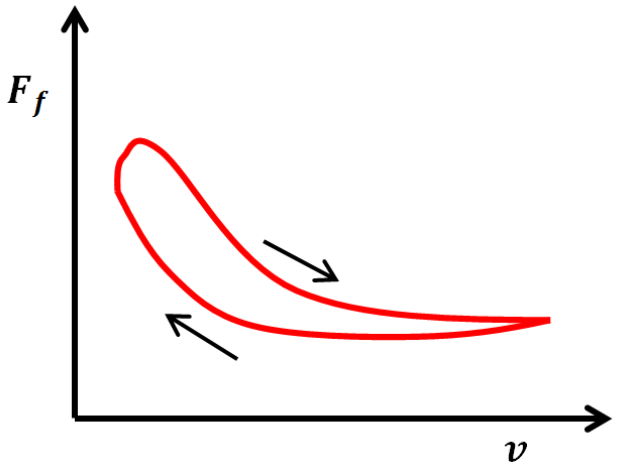

Figure 2.11: Frictional Lag - Friction versus velocity curve

2.3.2.1.1.6 Miscellaneous dependencies Experimentally, it has been found that friction show dependencies on following factors as well [41]

1. **Direction-dependent Friction** force typically vary for opposite direction of the interface velocity. For the same system, different numerical values are obtained for static friction parameters for opposite velocity directions.

2. **Position-dependent Friction** also show dependencies on position. The behavior is caused by irregularity of spatial conditions like varying contact geometry or different normal loads altering true contact area between the surfaces.

3. **Time-dependent Friction** in system is found to vary with time as well. This behavior occurs because of change in conditions at the interface like loss of lubrication, deformation at the interface, change in temperature and any accumulation of third particle body at the interface.

2.3.2.1.2 Classical Models In literature, friction can be modeled using different mathematical models that can capture few of the above mentioned friction phenomenon using information of interface velocity. With efforts of different researchers in classical mechanics, friction can be modeled using different terminologies.

2.3.2.1.2.1 Coulomb Friction Coulomb friction also known as kinetic or dynamic friction is proportional to the normal force at the contact interface and always acts in opposite direction to the relative motion of interface. It is independent of the area of contact. Mathematically, it is modeled as discontinued function as

$$\begin{aligned} F_f &= F_c sign(v) \\ F_c &= \mu \left| f_n \right| \end{aligned} \tag{2.6}$$

where μ is the coefficient of friction between the sliding surfaces and f_n is the normal force. F_c is the Coulomb Friction and F_f is the friction force. The term $sign(v)$ is the sigmoid function. This function introduces discontinuity which is difficult to tackle during numerical simulations, specially to determine exactly when velocity should be considered zero numerically. Typical Coulomb friction behavior is shown in Figure 2.12.

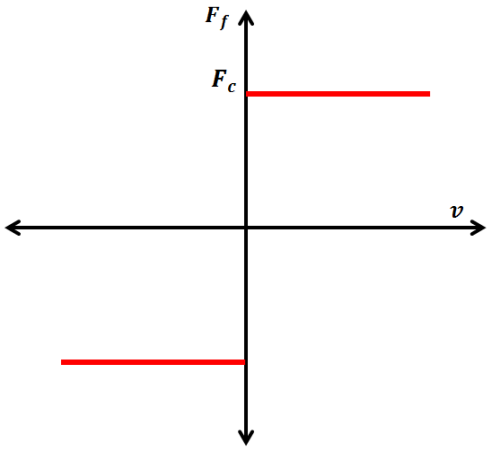

Figure 2.12: Coulomb Friction Behavior

2.3.2.1.2.2 Stiction Stiction is the static friction parameter which opposes external force at rest. It is greater than coulomb friction. Mathematically it is given by

$$F_f = \begin{cases} F_e & if \quad v = 0 \quad and \quad |F_e| < F_s \\ F_s sign(F_e) & if \quad v = 0 \quad and \quad |F_e| \geq F_s \end{cases} \tag{2.7}$$

where F_e is the external applied force and F_s is the Stiction/Static Friction force.

2.3.2.1.2.3 Viscous Friction Viscous friction arises due to development of full fluid lubrication film between the two sliding surfaces. Mathematically, this friction can be modeled using linear function of velocity

$$F_f = F_v v \tag{2.8}$$

where F_v is viscous friction coefficient. Graphically, viscous behavior is shown as a linear curve in Figure 2.13.

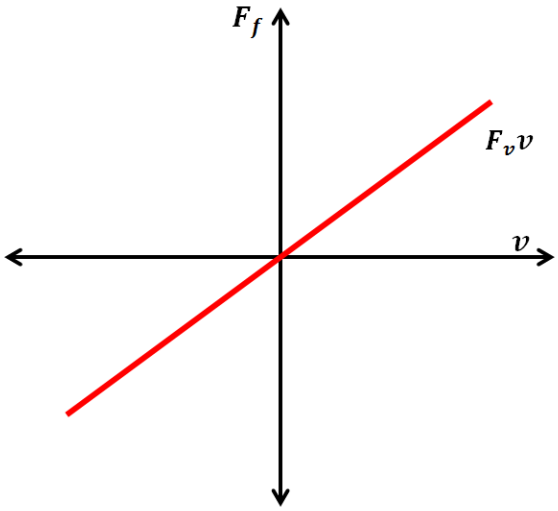

Figure 2.13: Viscous Friction Behavior

2.3.2.1.2.4 Stribeck Effect Stribeck effect as previously described, explains reduction in friction force during low velocity regime. This effect is being modeled using

$$F_f = (F_s - F_c) * e^{-|v/v_s|^\gamma} \tag{2.9}$$

where v_s is stribeck coefficient and γ is the tuning parameter. Graphically, stribeck friction can be represented as shown in Figure 2.14.

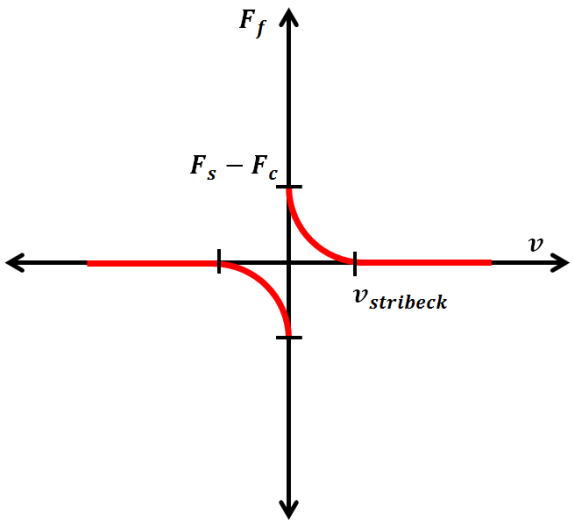

Figure 2.14: Stribeck Friction Behavior

2.3.2.1.2.5 CSVS friction model A more general static model is often used in literature that is based on coulomb, static, viscous and stribeck friction parameters. The

model is given mathematically as

$$F = \begin{cases} F(v) & if \quad v \neq 0 \quad and \quad |F_e| < F_s \\ F(e) & if \quad v = 0 \quad and \quad |F_e| < F_s \\ F_s sign(F_e) & otherwise \end{cases} \tag{2.10}$$

where $F(v)$ is given by

$$F(v) = F_c + (F_s - F_c)e^{-\left|\frac{v}{v_s}\right|^{\gamma}} + F_v v \tag{2.11}$$

Graphically, the friction predicted by CSVS friction model has characteristic curve as shown in Figure 2.15.

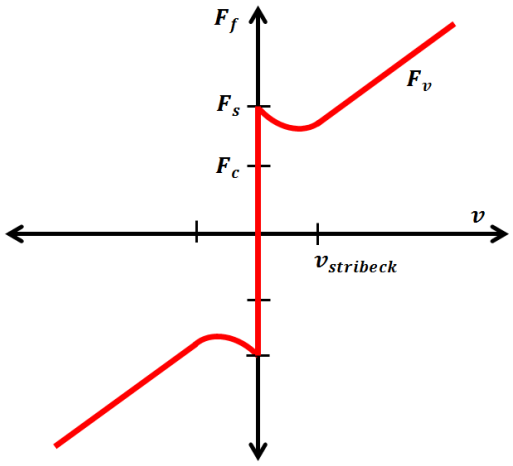

Figure 2.15: CSVS Friction Behavior

2.3.2.1.3 Dynamic Model Dynamic models consider friction with time dependent memory effects and captures complex phenomenon like pre-sliding displacement, frictional lag, varying breakaway force and stick-slip motion. They include Bristle model, Dahl model, LuGre model and Leuven model [2]. Here only LuGre model is presented as it is widely used in literature.

2.3.2.1.3.1 LuGre Model LuGre model was developed by collaboration efforts of researchers from Lund Institute of Technology(Sweden) and Grenoble France. It is one of the bristle models that explains the asperities at contact interface as bristles. The contact between two bodies is visualized as interaction between elastic bristles on both surfaces as shown in Figure 2.16. When a tangential force is applied, these bristles

deflect like springs and friction force appears.

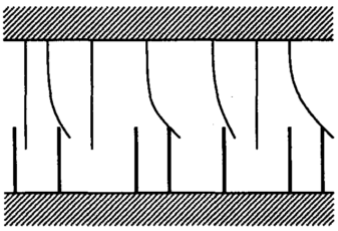

Figure 2.16: Contact interface considered as interaction between bristles on both surfaces [21]

If external force is large enough then few of the bristles deflect so much that slippage will occur at the interface. During the process new contact interfaces will be made. The whole process at microscopic level is very random because of irregular nature of the bristle interface. The model considers average behavior of bristles and gives force as average deflection force of elastic springs. The model is given by [21]

$$\frac{dz}{dt} = v - \sigma_0 \frac{|v|}{g(v)} z \tag{2.12}$$

$$F_f = \sigma_0 z + \sigma_1 \frac{dz}{dt} + F_v v \tag{2.13}$$

where F_f is the friction force at interface, z is the internal friction state, or microscopic displacement, v is the relative velocity of interface at macroscopic level, σ_0 is the average bristle stiffness at the interface, σ_1 is damping coefficient at microlevel, F_v is viscous friction coefficient.

$g(v)$ is parameter which includes stribeck effect and is given by

$$g(v) = F_c + (F_s - F_c) e^{-(v/v_s)^2} \tag{2.14}$$

where, F_c, F_s represents coulomb, static friction parameters and $v_s$represents stribeck velocity coefficient.

The model captures most of the friction behaviors that are observed experimentally which includes stick slip motion, rate dependency, pre-sliding displacement, hysteresis and frictional lag [40].

2.3.2.2 Backlash

Backlash is indeed a complex phenomenon, which include free motion dynamics in backlash mode, impact dynamics at the time of switching from backlash to contact mode and finally multi-body dynamics in contact mode.

Backlash is the free play between adjacent movable components within a mechanical system. For allowing relative motion between parts, backlash is an inevitable reality. Backlash is more prominent in system where forces directions are continuously reversed. Amount of backlash affects both system precision and dynamic behavior. Backlash is modeled by two widely used techniques; Dead-band effect and Impact dynamics during backlash collide. Dead band effect models backlash as a hysteresis behavior. Dead band is the region of input motion in mechanism for which there is no appreciable output motion.

2.3.2.2.1 Physical dynamics In order to understand backlash dynamics, consider the system as shown in Figure 2.17. The system consists of two inertia free shafts being coupled by an interface having backlash of magnitude 2α. Input shaft has stiffness k and viscous damping c.

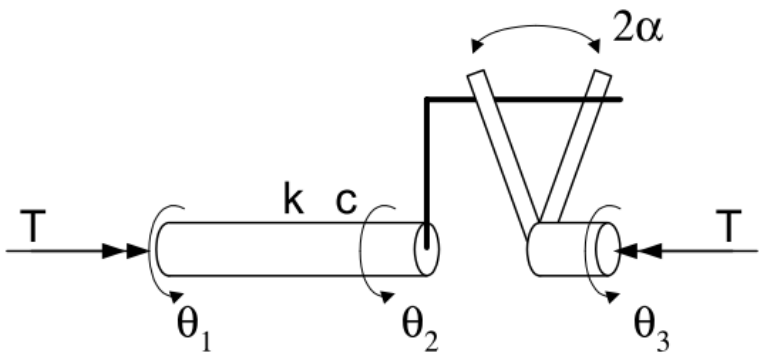

Figure 2.17: Backlash Schematics [29]

The transmitted torque equation is given by

$$T = k\theta_s + c\dot{\theta}_s = k(\theta_d - \theta_b) + c(\dot{\theta}_2 - \dot{\theta}_1) \tag{2.15}$$

where, $\theta_s = \theta_d - \theta_b$, $\theta_d = \theta_1 - \theta_3$, $\theta_b = \theta_2 - \theta_3$

2.3.2.2.2 Dead-Zone model In literature, dead-zone model is the most widespread backlash model. It considers the two rotating shafts as springs without any inertia and internal damping. It can be simply given by

$$T = \begin{cases} k(\theta_d - \alpha) & \theta_d > \alpha \\ 0 & |\theta_d| < \alpha \\ k(\theta_d + \alpha) & \theta_d < -\alpha \end{cases} \tag{2.16}$$

where T is the shaft torque, $\theta_d = \theta_1 - \theta_3$is the displacement in the backlash zone $\alpha$is half the backlash gap and k is the shaft stiffness. A typical transmitted torque curve as a function of backlash gap is given in Figure 2.18.

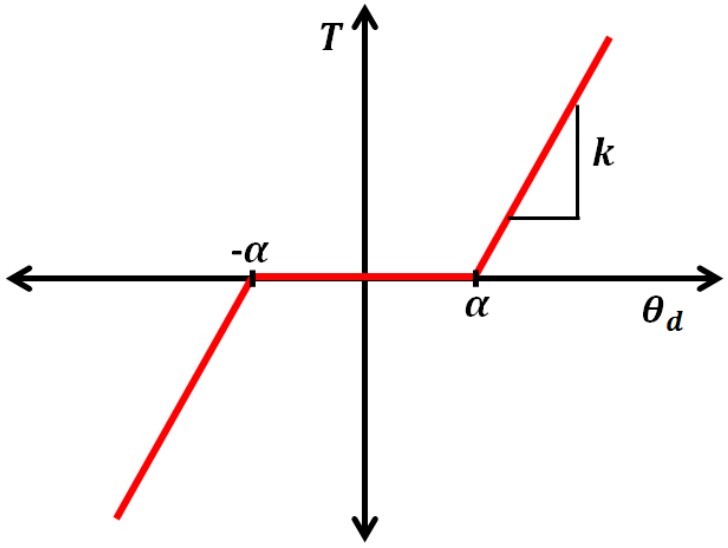

Figure 2.18: Transmitted torque as per Dead-zone model

2.3.2.2.3 The Hysteresis model This model relates input shaft angle to output shaft angle while assuming that both the shafts are stiff. For zero-disturbance load torque, the hysteresis model is given by

$$\dot{\theta}_3 = \begin{cases} \dot{\theta}_1(t) & if \quad \dot{\theta}_1(t) > 0 \quad and \quad \theta_3(t) = \theta_1 - \alpha \\ \dot{\theta}_1(t) & if \quad \dot{\theta}_1(t) < 0 \quad and \quad \theta_3(t) = \theta_1 + \alpha \\ 0 & otherwise \end{cases} \tag{2.17}$$

Equation 2.17 is referred as friction driven hysteresis model. The driven member during backlash mode retains its position because of assumption of strong friction force.

The behavior of friction driven hysteresis model is shown in Figure 2.19.

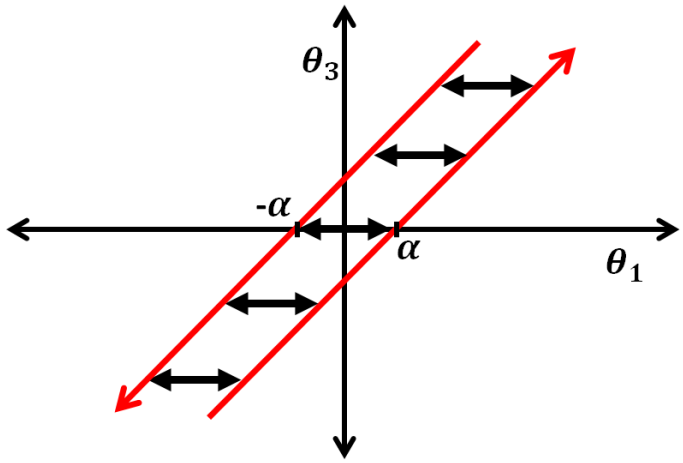

Figure 2.19: Friction driven hysteresis model

Inertial driven hysteresis model is alternative to friction driven model which assumes that driven member during backlash mode moves with same velocity without any friction force. Mathematically, the model is given by

$$\left.\begin{array}{llllll} \dot{\theta}_3(t) = \dot{\theta}_1(t) & if & \dot{\theta}_1(t) > 0 & and & \theta_3(t) = \theta_1 - \alpha \\ \dot{\theta}_3(t) = \dot{\theta}_1(t) & if & \dot{\theta}_1(t) < 0 & and & \theta_3(t) = \theta_1 + \alpha \\ \ddot{\theta}_3(t) = 0 & otherwise & & & \end{array}\right\} \quad (2.18)$$

Chapter 3

System Modeling

3.1 Physical System

Pan-tilt platform, a two axis gimbal assembly, can be represented as shown in Figure 3.1. The assembly is shown in a partially symmetric and balanced configuration. The system contains two rigid bodies (pan and tilt rigid body) and a grounded base. Both rigid bodies are connected by two revolute joints at different locations. Pan rigid body is connected with the grounded base; while tilt rigid body is mounted on pan rigid body.

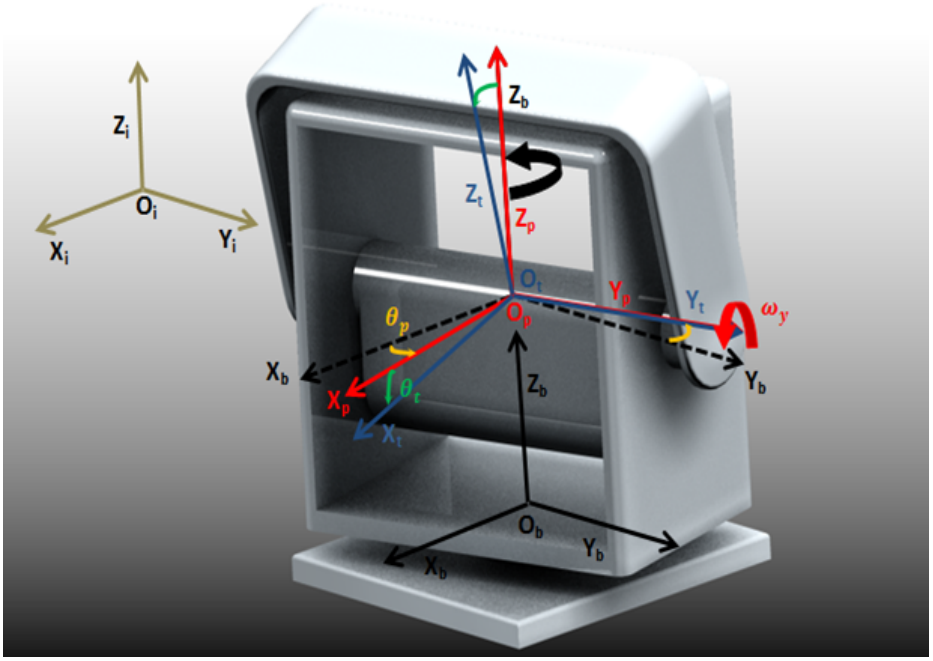

Figure 3.1: Pan-tilt platform with the necessary reference coordinates and Euler angles [8]

Following is the nomenclature for the system. Reference coordinate $O_iX_iY_iZ_i$ is assumed to be inertial frame. Marker B (for grounded base) is attached at the base of the assembly with O_b as origin and X_b, Y_b, Z_b as the direction axes. Marker P is attached at the mass center of the pan rigid body has O_p as origin and its directions axes (X_p, Y_p, Z_p) are aligned with the pan body principal axes. Similarly, Marker T is attached at the mass center of tilt rigid body, with O_t as origin and its direction axes (X_t, Y_t, Z_t) are aligned with tilt body principal axes.

Pan rigid body is connected with grounded base by pan revolute joint. This joint motion is captured by Marker Pj. It has O_{pj}as origin and X_{pj}, Y_{pj}, $Z_{pj}$are the direction axes. It can rotate about Z_b through an angle θ_p when external torque is applied. Marker B acts as the hard point for the pan revolute joint Marker P_j. Marker P and P_j has same angular velocity and they are related by geometric linear transformation.

Tilt rigid body is mounted on pan rigid body with tilt revolute joint. In order to keep description simple, it is assumed that hard point for tilt revolute joint is being provided by Marker P. Marker T also acts as a tilt revolute joint marker. It can rotate about Y_p through an angle θ_t when external torque is applied. ω_x, ω_y and ω_z are angular velocities of tilt rigid body whereas Euler angle rates ($\dot{\theta}_p$ and $\dot{\theta}_t$) are the input angular velocities at the respective input axis. ω_X, ω_Y and ω_Z are the angular velocities of tilt rigid body that appear on the inertial reference frame $O_iX_iY_iZ_i$.

3.1.1 System Dynamics

System constraints only allow two rotating reference frames; P and T. It is desirable to relate different motions in system using transformation. Kinematic transformations relate Euler angle rates ($\dot{\theta}_p$ and $\dot{\theta}_t$) to the tilt body angular velocities (ω_x, ω_y and ω_z); and finally transform tilt body angular velocities in the inertial frame.

Different Euler angle rates and body frame T angular velocities are shown in Figure 3.2 for better visualization of the different flows. These flows are related by following equations

$$\begin{aligned} \omega_x &= -\dot{\theta}_p \sin(\theta_t) \\ \omega_y &= \dot{\theta}_t \\ \omega_z &= \dot{\theta}_p \cos(\theta_t) \end{aligned} \tag{3.1}$$

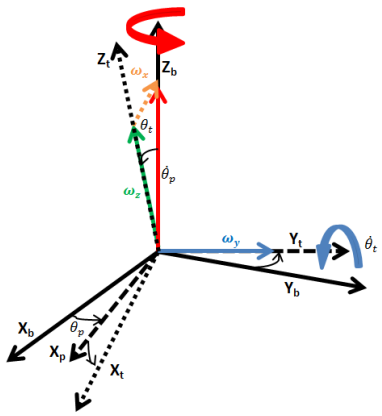

Figure 3.2: Angular velocities of body frames P and T [8]

It will be helpful to represent system dynamics using system equations. These equations are derived from scalar bond graph model of a balanced PTP which is obtained by reducing scalar bond graph model of three axis gimbal assembly [4] to two axis gimbal assembly. The reduced bond graph model is shown in Figure 3.3.

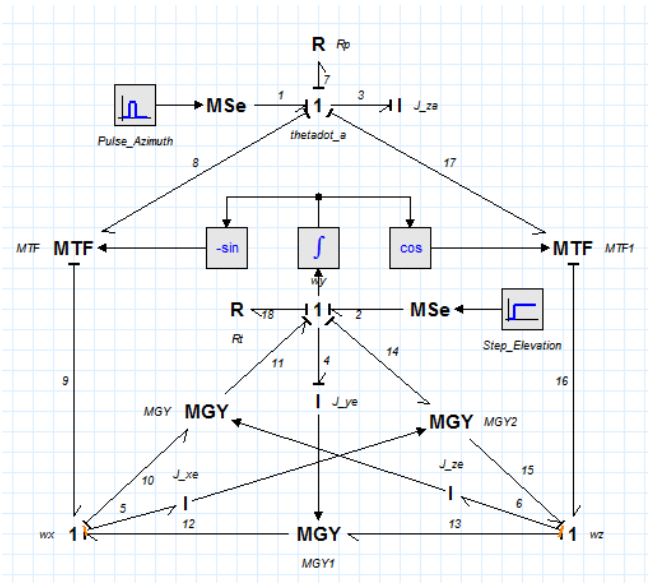

Figure 3.3: Scalar bond graph model of PTP - reduced from three axis platform model [4]

Pan velocity for pan and tilt inertial element is given by

$$\dot{\theta}_p = \frac{p_3}{J_{zp}} \tag{3.2}$$

$$\dot{\theta}_t = \frac{p_4}{J_{yt}} \tag{3.3}$$

From bond graph model (Figure 3.3), following flow equation can be written

$$f_1 = f_7 = f_8 = f_{17} = f_3 = \dot{\theta}_p$$

$$f_2 = f_4 = f_{11} = f_{14} = f_{18} = \dot{\theta}_t = \omega_y$$

Efforts $e_1$and e_2 represents input torques at pan and tilt joint respectively. Equations for the two friction elements are given by

$$e_7 = b_p \dot{\theta}_p$$

$$e_{18} = b_t \dot{\theta}_t$$

where b_7 and b_{18} represents viscous damping coefficients of pan and tilt revolute joints respectively. Flow equations from the two MTF's can be written as

$$f_9 = -\dot{\theta}_p \sin\theta_t = \omega_x$$

$$f_{16} = \dot{\theta}_p \cos\theta_t = \omega_z$$

Further flow relations can be written as follows

$$f_5 = f_{12} = f_{10} = f_9 = \omega_x$$

$$f_{15} = f_6 = f_{13} = f_{16} = \omega_z$$

Efforts for gyrators can be written as follows

$$e_{11} = J_{zt}\omega_z\omega_x \; ; \; e_{10} = J_{zt}\omega_z\omega_y$$

$$e_{12} = J_{yt}\omega_y\omega_z; \; e_{13} = J_{yt}\omega_y\omega_x$$

$$e_{14} = J_{xt}\omega_x\omega_z \; ; \; e_{15} = J_{xt}\omega_x\omega_y$$

Momentum equations for differentially causaled inertial elements are given by following relationships

$$p_5 = J_{xt}\omega_x = J_{xt}\left(-\sin\theta_t\dot{\theta}_p\right)$$

$$p_6 = J_{zt}\omega_z = J_{zt}\left(\cos\theta_t\dot{\theta}_p\right)$$

Other important efforts are given by

$$e_8 = -e_9 \sin\theta_t$$

$$e_9 = e_{10} + e_5 - e_{12}$$

$$e_{17} = e_{16} \cos\theta_t$$

$$e_{16} = e_{13} + e_6 - e_{15}$$

Effort given by the differentially causaled inertial elements due to attained angular velocities is given by

$$e_5 = \dot{p_5} = J_{xt} \frac{d\left(-\sin\theta_t \dot{\theta_p}\right)}{dt} = J_{xt} \left(-\cos\theta_t \dot{\theta_t} \dot{\theta_p} - \frac{\sin\theta_t}{J_{zp}} e_3 \right)$$

$$e_6 = \dot{p_6} = J_{zt} \frac{d(\cos\theta_t \dot{\theta_p})}{dt} = J_{zt} \left(-\sin\theta_t \dot{\theta_t} \dot{\theta_p} + \frac{\cos\theta_t}{J_{zp}} e_3 \right)$$

Effort summation equations at 1 junctions of integrally causaled inertial elements are given by

$$e_3 = \dot{p_3} = e_1 - e_7 - e_{17} - e_8 \tag{3.4}$$

$$e_4 = \dot{p_4} = e_{11} + e_2 - e_{18} - e_{14} \tag{3.5}$$

By putting values in Equation 3.4 and solving for e_3 will give

$$e_3 = \frac{J_{zp}\left(e_1 - b_p \dot{\theta_p} - 2J_{xt} \cos\theta_t \sin\theta_t \dot{\theta_t} \dot{\theta_p} + 2J_{zt} \cos\theta_t \sin\theta_t \dot{\theta_t} \dot{\theta_p}\right)}{J_{zp} + J_{zt} \cos^2\theta_t + J_{xt} \sin^2\theta_t}$$

$$\left(J_{zp} + J_{zt} \cos^2\theta_t + J_{xt} \sin^2\theta_t\right) e_3 = J_{zp}\left(e_1 - b_p \dot{\theta_p} - 2J_{xt} \cos\theta_t \sin\theta_t \dot{\theta_t} \dot{\theta_p} + 2J_{zt} \cos\theta_t \sin\theta_t \dot{\theta_t} \dot{\theta_p}\right) \tag{3.6}$$

Similarly by putting values in Equation 3.5 and solving for e_4 will give

$$e_4 = e_2 - b_t \dot{\theta_t} + J_{xt} \cos\theta_t \sin\theta_t \dot{\theta_p}^2 - + J_{zt} \cos\theta_t \sin\theta_t \dot{\theta_p}^2 \tag{3.7}$$

$$e_3 = \dot{p_3} = J_{zp} \ddot{\theta_p}$$

$$e_4 = \dot{p_4} = J_{yt} \ddot{\theta_t}$$

Above derived equations can be written in following matrix form,

$$\begin{bmatrix} 1 & 0 & 0 \\ 0 & J_{yt} & 0 \\ 0 & 0 & J_{zp}+J_{zt}\cos^2\theta_t+J_{xt}\sin^2\theta_t \end{bmatrix} \begin{Bmatrix} \dot{\theta}_t \\ \ddot{\theta}_t \\ \ddot{\theta}_p \end{Bmatrix}$$
$$= \begin{bmatrix} 0 & 1 & 0 \\ 0 & -b_t & \cos\theta_t \sin\theta_t \dot{\theta}_p (J_{xt}-J_{zt}) \\ 0 & -2J_{xt}\cos\theta_t \sin\theta_t \dot{\theta}_p & -b_p+2J_{zt}\cos\theta_t \sin\theta_t \dot{\theta}_t \end{bmatrix} \begin{Bmatrix} \theta_t \\ \dot{\theta}_t \\ \dot{\theta}_p \end{Bmatrix} + \begin{bmatrix} 0 & 0 \\ 0 & 1 \\ 1 & 0 \end{bmatrix} \begin{Bmatrix} e_1(t) \\ e_2(t) \end{Bmatrix} \tag{3.8}$$

By substituting, $\theta_t = x_1$, $\dot{\theta}_t = x_2$ and $\dot{\theta}_p = x_3$, Equation 3.8 can be written as

$$\begin{bmatrix} 1 & 0 & 0 \\ 0 & J_{yt} & 0 \\ 0 & 0 & J_{zp}+J_{zt}\cos^2 x_1+J_{xt}\sin^2 x_1 \end{bmatrix} \begin{Bmatrix} \dot{x_1} \\ \dot{x_2} \\ \dot{x_3} \end{Bmatrix}$$
$$= \begin{bmatrix} 0 & 1 & 0 \\ 0 & -b_t & x_3\cos x_1 \sin x_1 (J_{xt}-J_{zt}) \\ 0 & -2J_{xt}x_3\cos x_1 \sin x_1 & -b_p+2J_{zt}x_2\cos x_1 \sin x_1 \end{bmatrix} \begin{Bmatrix} x_1 \\ x_2 \\ x_3 \end{Bmatrix} + \begin{bmatrix} 0 & 0 \\ 0 & 1 \\ 1 & 0 \end{bmatrix} \begin{Bmatrix} e_1(t) \\ e_2(t) \end{Bmatrix}$$

where J_{xt}, J_{yt} and J_{zt} are principal moments of inertia of tilt body; J_{xp}, J_{yp} and J_{zp} are principal moments of inertia of pan body . It is interesting to note here, that θ_p is not a state variable since its initial value has no impact on system dynamics. Moreover, system dynamics reduced to balanced rotating tilt body if no input is given in pan axis.

3.2 System Modeling

Using advantage of Multi-bond graph technique based on Object Oriented Modeling approach system modeling is carried out in stepwise manner.

3.2.1 Ideal PTP

Ideal PTP model is built without considering any mechanical imperfection in the system. The system is assumed in partially symmetric and balanced configuration as shown in Figure 3.1. Control strategy demands position and velocity control of system therefore, sources of flow with desired motion profiles is attached at the revolute joints.

Building system model from basic components, already modeled using OOM approach only requires topology information. PTP has four main components; two revolute joints and two rigid bodies. Pan revolute joint is between grounded base and pan rigid body and tilt revolute joint is between tilt rigid body and pan rigid body. Figure 3.4 shows MBG model of PTP in which different system components are connected using system topology.

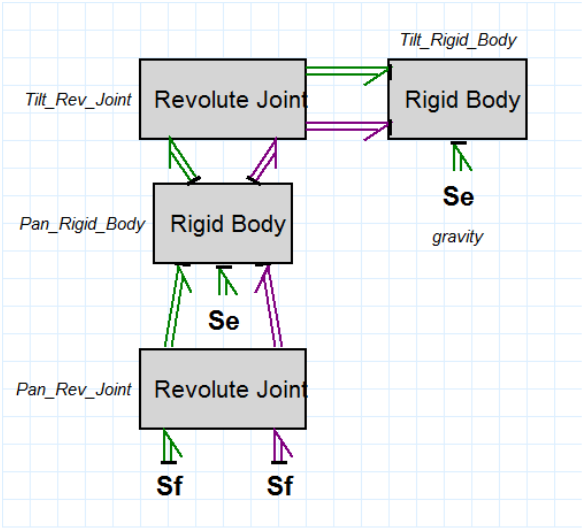

Figure 3.4: Multi-Bond Graph model of PTP using Object Oriented Modeling approach [8]

In Figure 3.4, sources of flows at pan revolute joint represents grounded base. Revolute joint details are shown in Figure 2.5 with source of effort being replaced by modulated source of flow. Figure 3.5 shows model of tilt rigid body. Details of encapsulated "Rigid Body Tilt" of Figure 3.5 are shown in Figure 2.3.

Transformation inside encapsulated "Body Rates to Euler Rates" is given by following equations [1]

$$\begin{aligned} \dot{\theta} &= cos\phi\,\omega_y - sin\phi\,\omega_z \\ \dot{\psi} &= \frac{sin\phi}{cos\theta}\omega_y + \frac{cos\phi}{cos\theta}\omega_z \\ \dot{\psi} &= \omega_x + sin\phi\frac{sin\theta}{cos\theta}\omega_y + cos\phi\frac{sin\theta}{cos\theta}\omega_z \end{aligned} \tag{3.9}$$

Euler angles are calculated by integrating Euler rates found in Equation 3.9. These Euler angles are used in transformation of revolute joints. Details of encapsulated

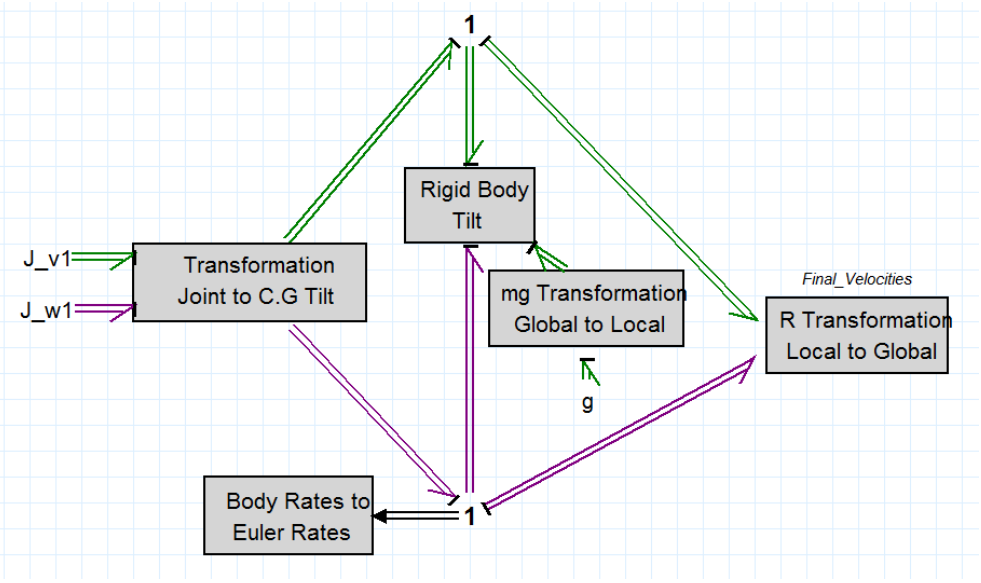

Figure 3.5: Tilt rigid body model[8]

"Transformation Joint to C.G Tilt" are shown in Figure 2.6. It can be seen that MBG model of PTP shows power exchange phenomenon among different elements while system topological information is retained.

3.2.2 PTP with Payload

Addition of payload to the ideal PTP model is to introduce mechanical imperfection of mass imbalance. System is converted to partially symmetric and unbalanced configuration. Physically, payload is mounted on tilt rigid body. This topological information is used to connect payload as rigid body by a rigid link (joint) with zero degree of freedom. Details of encapsulated "Payload" in Figure 3.6 are similar to details in Figure 2.3.

It can be seen that payload is added to the ideal PTP model quite similar the way it happens in physical system. No equations were derived for building bond graph model for the modified system.

3.2.3 PTP with Actuators

PTP has two independent actuators for pan and tilt axes. Considered PTP configuration is supposed to carry high payloads (with appreciable c.g offset) with low flow rates

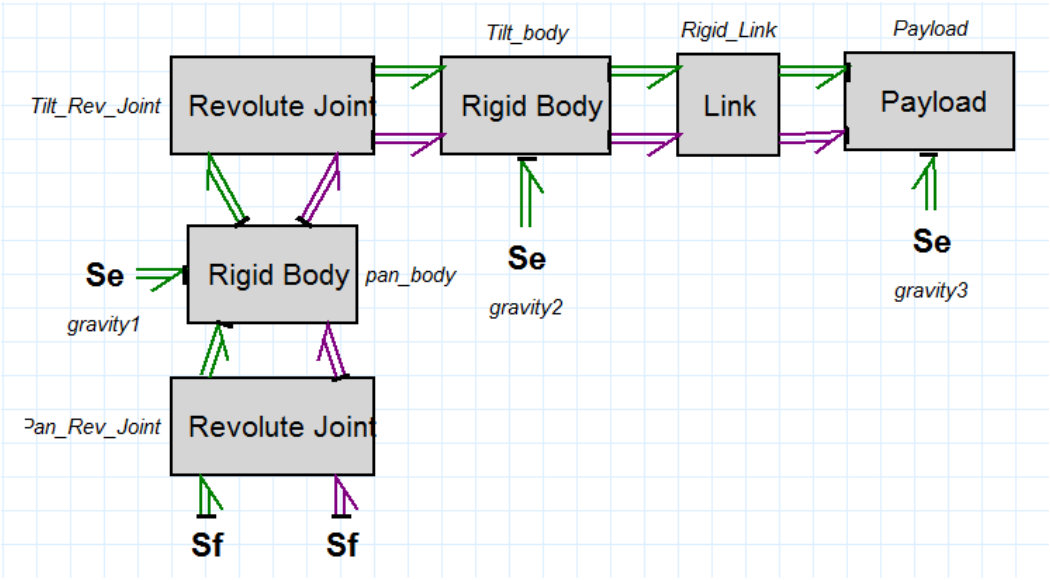

Figure 3.6: MBG model of PTP-Payload using OOM approach[8]

in tilt axis whereas variable flow rates are expected in pan motion. For pan motion, implementation of controls using micro-controller is essential for accurate position and velocity control whereas for tilt motion, only position control is required which can be done by using potentiometer. Pan joint actuation details of servo-mechanism is added by modeling PMDC gear motor with PID controller. Tilt actuation is modeled by using linear actuator powered by a PMDC motor.

3.2.3.1 Pan Motion Actuation

In physical system, pan motion is actuated by geared Permanent Magnet DC(PMDC) motor. The motor is being controlled by PID control strategy, implemented using micro-controller LM-629. The feedback is done by using incremental encoder with 7200 counts/rev. The mathematical equation for electrical domain modeling of the motor is given by,

$$L_e \frac{di}{dt} + iR_e + K_t \omega_m = u \tag{3.10}$$

where $L_e$is the coil inductance, i is the current in the coil, $R_e$is the coil resistance, $K_t$is the motor torque constant, ω_m is the angular velocity of the motor, u is the control input of the system. Similarly, mechanical domain equation can be written as,

$$K_t i = J_m \frac{d^2\theta_m}{dt^2} + \frac{1}{N^2}(F_f + J_l \frac{d^2\theta_m}{dt^2} + k_s(\theta_m - N\theta_l)) \tag{3.11}$$

where J_m and J_l are the motor and load inertia, θ_m and θ_l is the angular displacement of motor and load, N is the gear ratio, F_f is the friction force and k_s is the shaft stiffness . Using Bond Graph, above equations can be represented as shown in Figure 3.7.

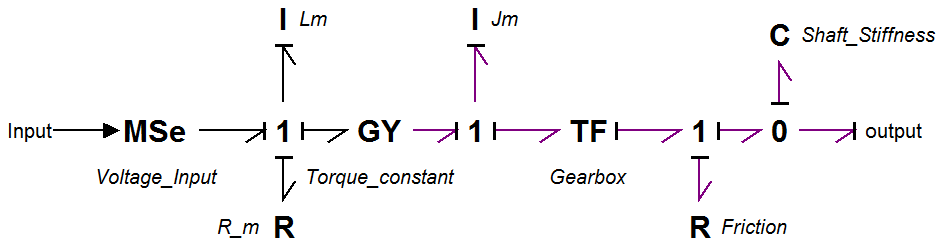

Figure 3.7: BondGraph Model of Geared PMDC motor

Details of PMDC motor is added in the MBG model of PTP by encapsulating PMDC motor as shown in Figure 3.8. Physically input to PMDC motor is given by using controller and its output at pan joint is given to the system using relevant mounting constraints. Complete details are encapsulated as servo-geared motor at the pan revolute joint.

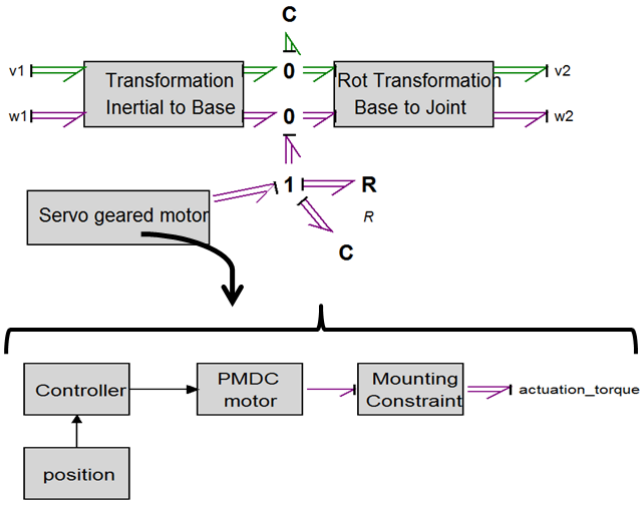

Figure 3.8: Servo-mechanism details at pan revolute joint

Controller details are shown in Figure 3.9. Motion profile gives desired velocity, PID box determines output based on the error of position . Output of PID is used to generate motor drive signal using PWM. PWM used in the model is the builtin 20-sim model.

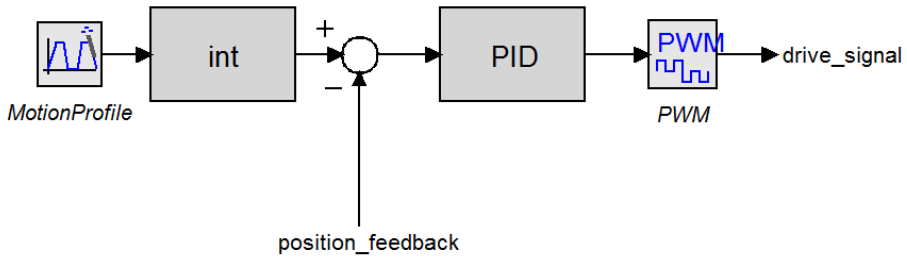

Figure 3.9: Controller details with PID controller and PWM drive

3.2.3.2 Tilt Motion Actuation

Linear actuator gives relatively high force with low velocity in compact geometry. The mechanism also provides self-locking which is key requirement in unbalanced tilt axis. Actuation is carried out by PM-DC motor with gearing, followed by lead screw and nut assembly. Cut-view details of a linear actuator is shown in Figure 3.10.

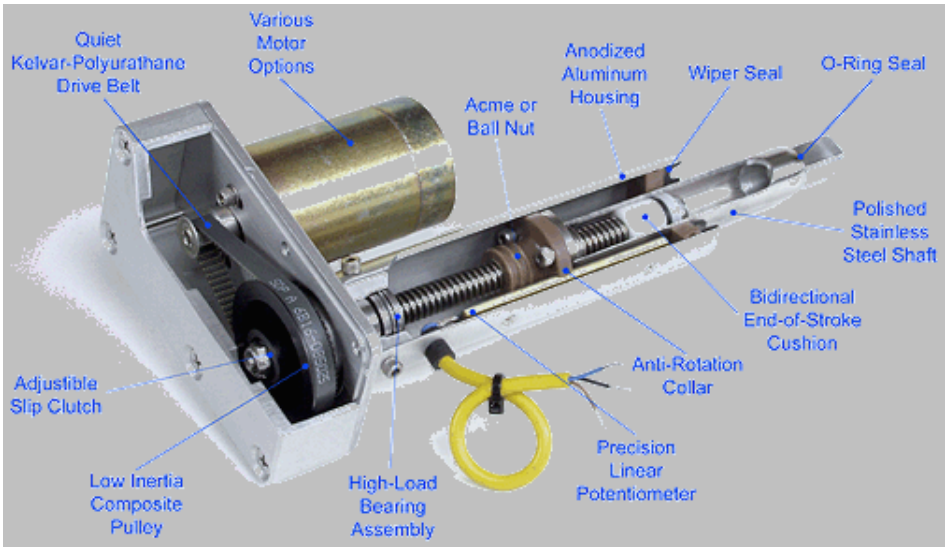

Figure 3.10: Cutview of a linear actuator [42]

Actuator extends/contracts its stroke and provides torque at tilt axis with the help of a mechanical linkage acting as moment arm. Details of Tilt mechanism with linear actuator is shown in Figure 3.11.

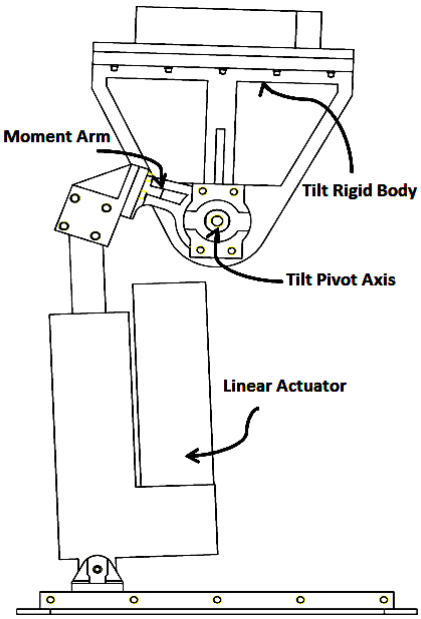

Figure 3.11: Tilt actuation mechanism in PTP Assembly

Bond graph model of linear actuator is shown in Figure 3.12. DC motor and its gearing mechanism is modeled in similar way as it was done in pan mechanism except that the motor shaft is assumed to be rigid; making motor as source of flow. Motor torque is being sensed back against the flow it generates using standard power screw equations. These equations are

$$\begin{aligned} T_{raise} &= \frac{Fd_m}{2}\left(\frac{l+\pi f d_m}{\pi d_m - fl}\right) \\ T_{lower} &= \frac{Fd_m}{2}\left(\frac{\pi f d_m - l}{\pi d_m + fl}\right) \end{aligned} \tag{3.12}$$

where F is the linear force that is required by the actuator, T is motor torque, d_m is mean diameter of lead screw, f is the coefficient of friction between screw and nut and l is the lead of the screw. These equations are implemented in transformer labeled as "LeadScrew" in Figure3.12.

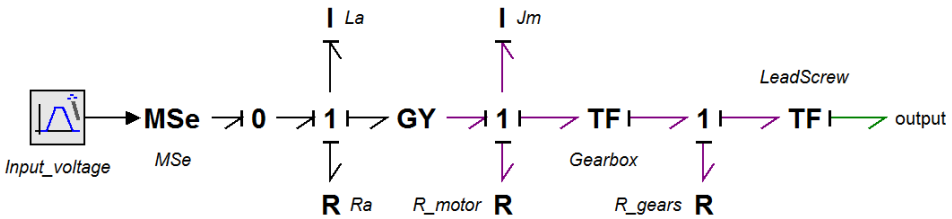

Figure 3.12: Bond Graph model of Linear Actuator

Linear actuator gives flow which is transformed into 3D assembly as angular velocity at tilt pivot axis. Force for linear actuator is calculated by sensing tilt torque. In

order to estimate transformations capturing dynamics of tilt actuation mechanism, different geometric identities are used. These are shown in Figure 3.13. Mechanism can be assumed as a three bar mechanism. Internal angles of the mechanism are estimated using following trigonometric relationship

$$\beta = \arccos\left(\frac{r^2 + l^2 - l_g^2}{2lr}\right)$$

where l is the length of actuator (sum of stroke l_s and minimum extracted length l_0), r is the moment arm, l_g is the third side of triangle comprising of ground vertical and horizontal components.

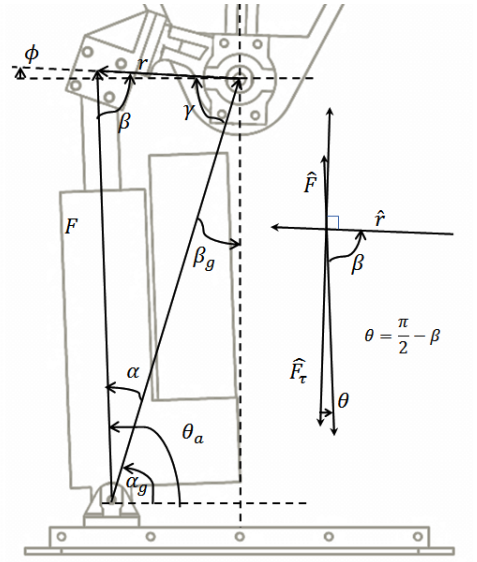

Figure 3.13: Linear Assembly with geometric identities

Linear actuator gives flow and receives effort information in the direction of motion of its stroke. The direction is shown as $\hat{F}$. The linear velocity is converted to angular velocity at tilt pivot joint using

$$\omega_{tilt} = -v_a/(r\cos\theta)$$

where $v_a$is linear actuator speed and $\theta$is the angle shown in Figure 3.13,and given by

$$\theta = \frac{\pi}{2} - \beta$$

Similarly, force which is felt by the actuator can be calculated by

$$F_a = -\tau_{tilt}\cos\theta/r$$

Modeling details of assembly mechanism is added to the model as shown in 3.14.

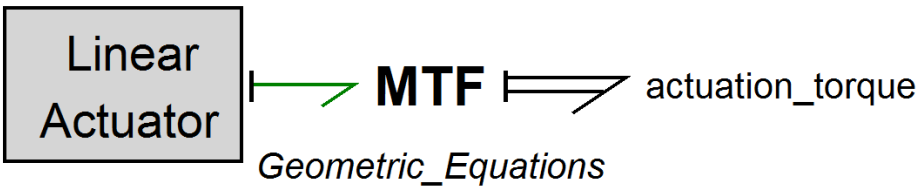

Figure 3.14: Linear actuator assembly

3.2.4 PTP with mechanical Imperfections

Among pan and tilt axes motion, mechanical imperfections are added in pan motion axis, since for considered PTP application, only pan position and velocity control is required. Mechanical imperfections of friction and backlash is added in the MBG model of PTP. Viscous friction model was already used in the ideal PTP model for providing system damping and stability of the solution. CSVS friction model is used as its parameters were successfully estimated from experimental results. The Friction is added as an R element with motor gearhead since most of the friction in pan joint exist there.

Backlash is being modeled using Deadzone model given by Equation 2.16, using bond graph methodology given by McBride [43]. It considers backlash as modulated source of effort and acts as two different springs in backlash and contact mode. Backlash detail is added in servomechanism as shown in the Figure 3.15.

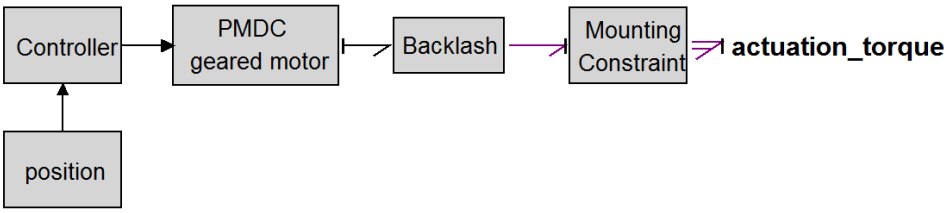

Figure 3.15: Backlash in pan servomechanism

Details inside backlash box is shown in Figure 3.16. Flows from load and motor are sensed and difference between their respective displacements is calculate to determine the backlash gap. Based on the calculation of backlash gap, stiffness of the spring is modulated inside source of effort (Mse).

Twist in transmission shaft is calculated as the difference between calculated position difference and the quantified backlash gap. It can be represented by following if else statements [43]

Algorithm 3.1 Twist logical statements

```
if(position_error > backlashgap/2) then
 Twist = (position_error -backlashgap/2)
elseif(position_error <-backlashgap/2) then
 Twist = (position_error + backlashgap/2)
else
 Twist = 0
end
```

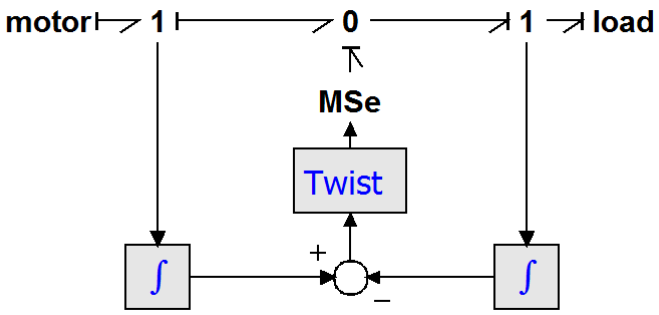

Figure 3.16: Backlash Model details

Chapter 4

Parameters Estimation

Experiments were conducted for estimating different parameters of backlash and friction models in first stage. In later stage, experiments were used to compare the PTP model. In this chapter, different experiments are discussed along with details for estimating parameters from the experimental data. Experiments are conducted on current PTP of NUST Ground Surveillance Radar.

4.1 Backlash quantification

For using backlash model explained in Section 3.2.4, backlash gap of pan joint is needed to be estimated. For its accomplishment, a simple experiment was conducted. The schematics of the experiment is shown in Figure 4.1.

Encoder reading is reset at one extreme of play and then the joint is manually rotated to the other extreme of the play. Encoder pulses are used to measure the displacement between the two extremes of the play. Readings at different locations of the joint were taken and finally an average value is used as estimated value for backlash gap or dead-zone width. Appendix A gives the measured values observed during experimentation. The average backlash gap is found to be 1.49 degrees.

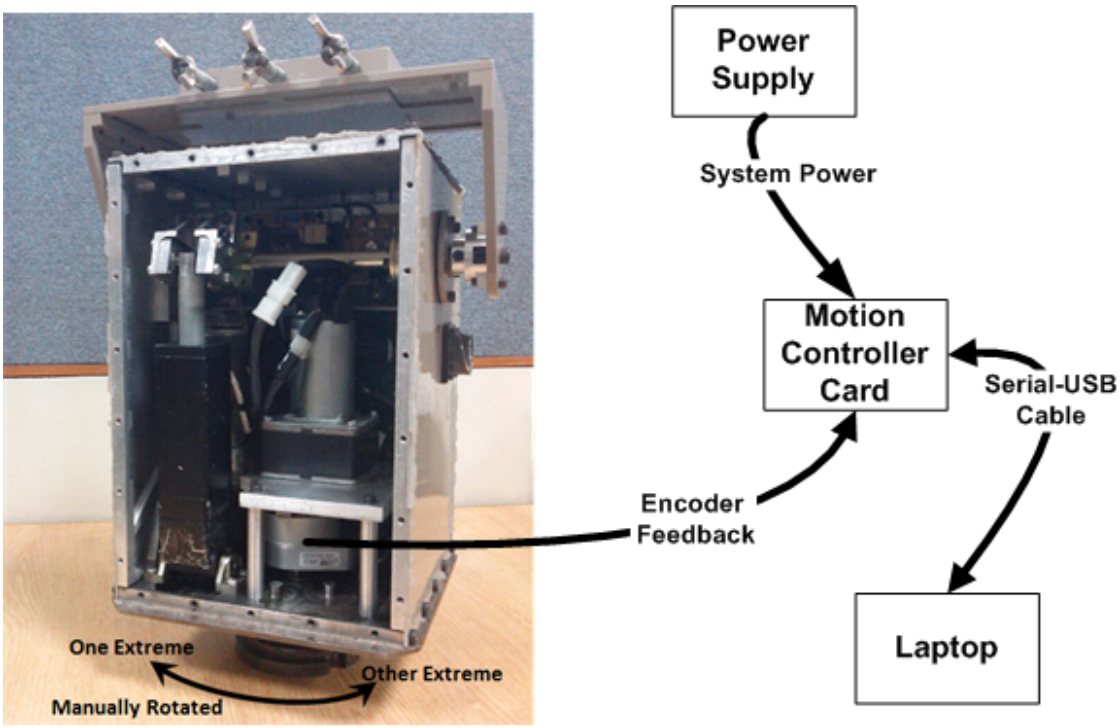

Figure 4.1: Schematics of Experiment for quantification of backlash gap

4.2 LuGre Friction Parameters

For using LuGre Friction model given by Equations 2.12 & 2.13, one need to estimate six friction parameters. Among them four are steady state parameters and other two are dynamic parameters. In literature, procedures for collecting different experimental data have been presented [44, 45]. Based on guidelines [44], different experiments were planned for collecting required data. Experimental data was then used to estimate LuGre friction model parameters by using MATLAB Optimization Toolbox.

4.2.1 Steady State Friction Parameters

Steady state friction parameters includes static friction coefficient F_s, Coulomb's friction coefficient F_c, Stribeck friction coefficient v_s and viscous friction coefficient F_v. These parameters can be estimated by creating a map between steady state velocity and steady state torque. Steady state velocity is read using incremental encoder mounted

at joint whereas torque is estimated by measuring the motor current. For conducting experiment a simple setup was planned. Its schematics is shown in Figure 4.2.

Motor current is being measured by the using Agilent power supply E3631A, which is also powering up the complete system. Motion controller card is connected by computer using serial-usb cable whereas Agilent Power supply is connected by computer using gbip-usb cable. Using MATLAB code, the desired steady state velocity is given to micro-controller. PTP is rotated in pan at desired constant velocity using PI control strategy. Average velocity reading and average power supply current reading is noted. Measured current reading also contains the current drawn by motion controller card. For estimating motor current, motion controller card current is noted before the start of the experiment and it is assumed that the card current doesn't change during motor operation. Motor current is estimated by subtracting motion controller current from the measured current. Motor torque is estimated by multiplying torque constant with the average motor current. Motor parameters are given by its manufacturer. Readings are taken for different steady state velocities in both clockwise and anticlockwise direction.

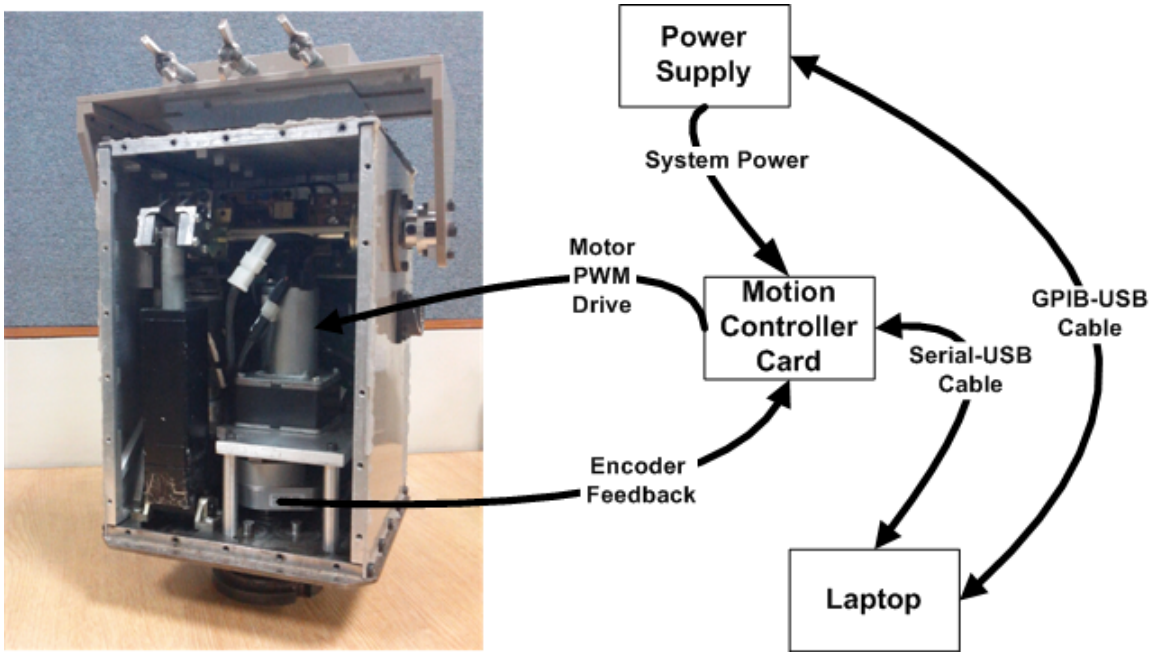

Figure 4.2: Schematics of Experiment for Estimation of Static Friction Parameters

After getting velocity-torque map for steady steady operation, steady state friction parameters are estimated using MATLAB Optimization Toolbox's built-in func-

tion lsqcurvefit. The function solves nonlinear data fitting problems by nonlinear least squares approach. The approach defines objective function as a sum of squares of the difference of all observed data point with the predicted data. Mathematically, objective function is given by [46]

$$\min_x \|F(x,xdata) - ydata\|^2 = \min_x \sum_i (F(x,xdata_i) - ydata_i)^2$$

where $ydata$ is the experimentally measured value of output variable. $F(x,xdata)$ is the function that predicts the output value which is compared with experimental data value or $ydata$. $F(x,xdata)$ is a function of $xdata$,the input variable and x, array containing parameters to be estimated. Initial values of parameters are used to find out the sum of residuals and then parameters are changed algorithmically so as to minimize the objective function. For minimizing objective function MATLAB has two algorithms; "trust-region-reflective" and "Levenberg-Marquardt" algorithms. Trust-region-reflective algorithm is used since MATLAB recommends it's use for the specific problem at hand i.e a bounded and an over-constraint system [46].

In the given system, $xdata$ is the input steady state velocity, $ydata$ is the steady state torque, $F(x,xdata)$ for the system is predicted by Equation 4.1

$$F_{ss} = (F_c + (F_s - F_c)exp^{-|\frac{v}{v_s}|^2}) * sign(v) + F_v v \tag{4.1}$$

where $v = xdata$ and four parameters (F_c, F_s, v_s and F_v) to be estimated are represented by the array x. "lsqcurvefit" uses equation 4.1 and experimental $ydata$ to find the residual of the two values. Then it changes parameters using marching algorithm so as to minimize the sum of squares of the residuals. Since the problem is non-linear therefore initial guess of parameter values is important. By using guidelines in the literature [44], initial parameters from the experimental data is estimated. Then different starting value sets for parameters are used around these guessed values. Parameters set giving minimum residual are selected as the estimated parameters for friction. Table 4.1 shows initial estimated values and finally the values that are estimated using "lsqcurvefit".

Table 4.1: Estimated Static Friction Parameters

Parameter	Initial values		Estimated Values	
	$\omega > 0$	$\omega < 0$	$\omega > 0$	$\omega < 0$
Coulomb Friction Coefficient F_c	0.53	0.65	0.2267	0.2535
Static Friction Coefficient F_s	0.6	0.82	0.5578	0.7922
Stribeck Friction parameter v_s	0.01	0.02	0.0159	0.0161
Viscous Friction Coefficient F_v	14.36	15.64	13.5844	14.3004

Experimental data and predicted steady state friction using estimated friction parameters are plotted in Figure 4.3.

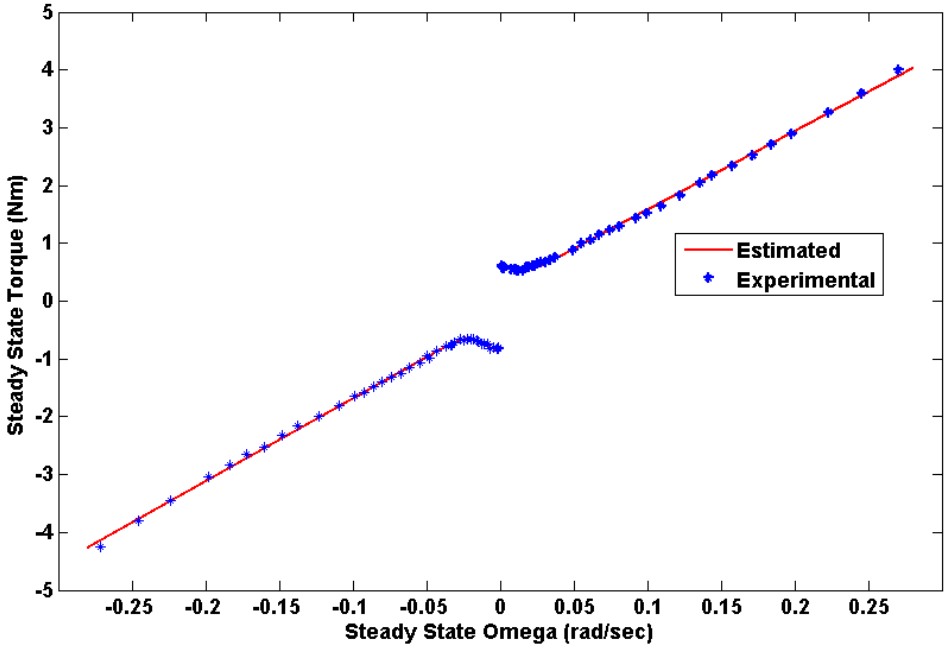

Figure 4.3: Experimental and Predicted Steady State Friction

4.2.1.1 Limitation of Experimental Setup

Typically data sampling equipment is used for measuring experimental variables and inputs. Because of unavailability of proper instrumentation, motor current is measured using improvised experimental setup. Agilent power supply which was used to power up the complete system was also used to estimate motor current while sampling at 3 Hz. PWM drive is given to the motor and it was assumed that the motor current doesn't vary much during the steady state run. Moreover, power supply current reading

also accounted for the current drawn by the motion controller card, therefore motion controller card reading was noted for no run state. It was assumed that controller current doesn't change during the steady state motor run. Finally, motor current is estimated by subtracting controller card current from steady state measured current.

4.2.2 Dynamic Friction Parameters

For calculating dynamic friction parameters, literature suggest a sine torque input. The torque input should be increased such that its peak value should be slightly higher than breakaway torque. Then by using Equations 2.12 & 2.13, the parameters σ_0 bristle stiffness and σ_1 bristle damping can be estimated with the help of lsqcurvefit function of MATLAB Optimization Toolbox. Load inertia J_l can also be estimated using this experimental data. But before starting parameter estimation, the procedure requires to guess the values of these parameters as the problem is highly non-linear. For doing this, two experiments in open loop are suggested [44]. First experiment, suggests to give a ramp input with very low slope and second experiment suggest to give a step input well below estimated static friction coefficient F_s. For accomplishing both experiments, high resolution encoders are must; generally in the range of 100,000 pulses/rev. Specially, in second experiment in which the system behaves like a second order LTI mass-spring-damper system. The step response to be captured is at microscopic level. The available encoder's resolution was not enough to conduct these experiments. Available encoder generates 1800 pulses/rev and with the help of micro-controller LM629, its resolution is enhanced four times. This resolution is way too less than the required value. As a result, it was concluded that dynamic parameters of LuGre friction model are not feasible to estimate using the available measurement setup. Since steady state parameters were estimated in Section 4.2.1, it was decided that CSVS friction model will be used in MBG model of PTP instead of LuGre friction model.

4.3 Moment of Inertia

Moment of Inertia was initially planned to be estimated during estimation of dynamic friction parameters. Since the estimation of dynamic friction parameters couldn't be accomplished (Section 4.2.2), so for estimating moment of inertia, another experiment

was planned. The setup was similar to the ramp input experiment suggested to guess $\sigma_0$bristle stiffness [44]. Similar setup is used for estimating viscous and coulomb friction [47]. The method [44] suggests an open loop experiment which was perceived as DC drive instead of PWM drive through micro-controller. DC drive was given to motor by Agilent power supply E3631A and angular displacement is measured using encoder. The schematics of the experimental setup is shown in Figure 4.4.

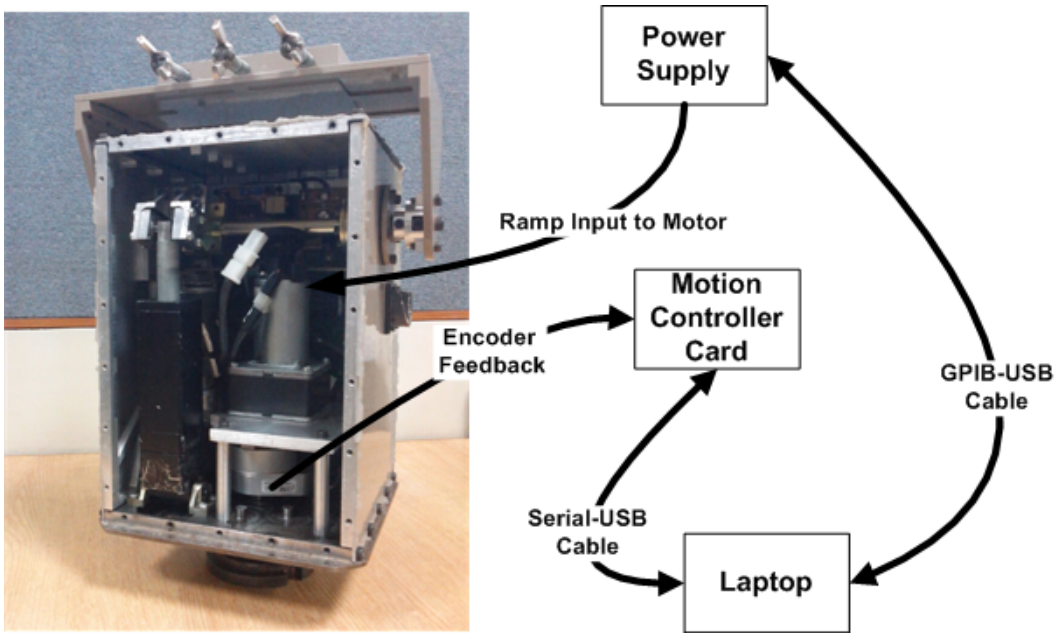

Figure 4.4: Schematics of Experiment for Estimation of Moment of Inertia

An initial guess for inertia was taken from PTP assembly drawings in Pro/Engineer. It was observed during the test, that there is a substantial difference in friction parameters of the pan joint and actuator while using different drives. The observed steady state friction parameters using dc drive are found quite high as compared to what were observed and estimated using PWM drive. For this reason, the experimentation data is not only used to estimate moment of inertia but also friction parameters. The system equation is given by

$$\hat{J}\frac{d^2x_m}{dt^2} = u - \hat{F}$$

where $\hat{J}$ is the estimated moment of inertia, $x_m$is the pan position numerically calculated by ode15s solver, u is the input torque and $\hat{F}$is the estimated friction calculated by equation 4.1, where velocity v_m from numerical model is used as $xdata$. Flowchart of calculations is being shown in Figure 4.5.

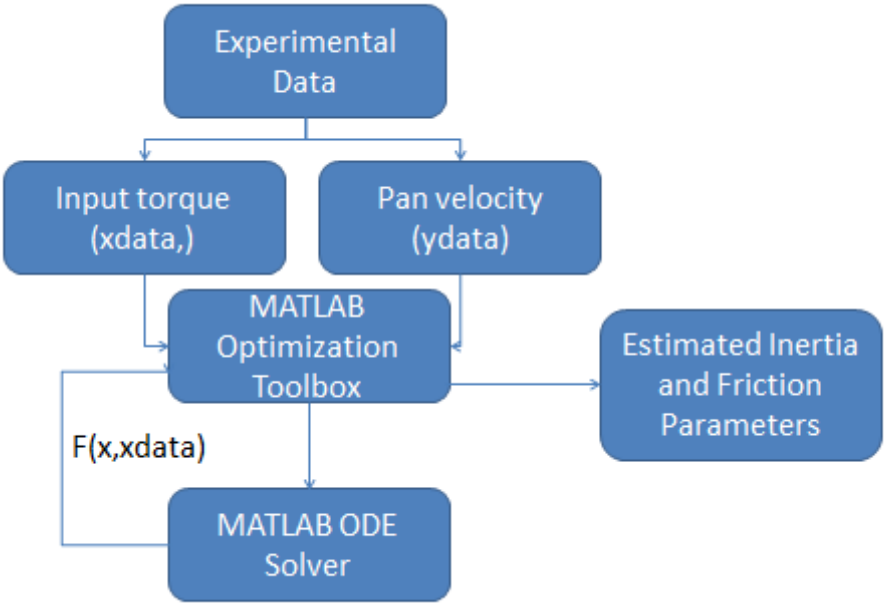

Figure 4.5: Data flow during Inertia estimation

The estimation is again done by using MATLAB Optimization Toolbox built-in function "lsqcurvefit". The results are tabulated and finally the average value is calculated which is found to be $0.050 kgm^2$.

Table 4.2: Estimated Values of Inertia and DC drive open loop friction

S.No	$\omega > 0$					$\omega < 0$				
	J	F_s	F_c	v_s	F_v	J	F_s	F_c	v_s	F_v
1	0.0503	7.203	5.936	0.0427	5.304	0.0495	6.504	5.354	0.0972	7.601
2	0.0504	7.511	5.699	0.0363	6.523	0.0497	8	5.001	0.0926	6.95
3	0.05	8.1	6.029	0.0492	5.483	0.0498	7.702	4.991	0.1096	5.835
4	0.05	7.81	5.89	0.0457	5.5	0.0499	7.298	5.372	0.1109	6.446
5	0.0506	6.6	5.549	0.0138	5.374	0.0501	7.771	5.791	0.066	5.334
Avg	0.0502	7.656	5.888	0.0434	5.70	0.0498	7.72	5.435	0.0844	6.101

Typical curve fitting of the simulated and experimental data is shown in Figure 4.6.

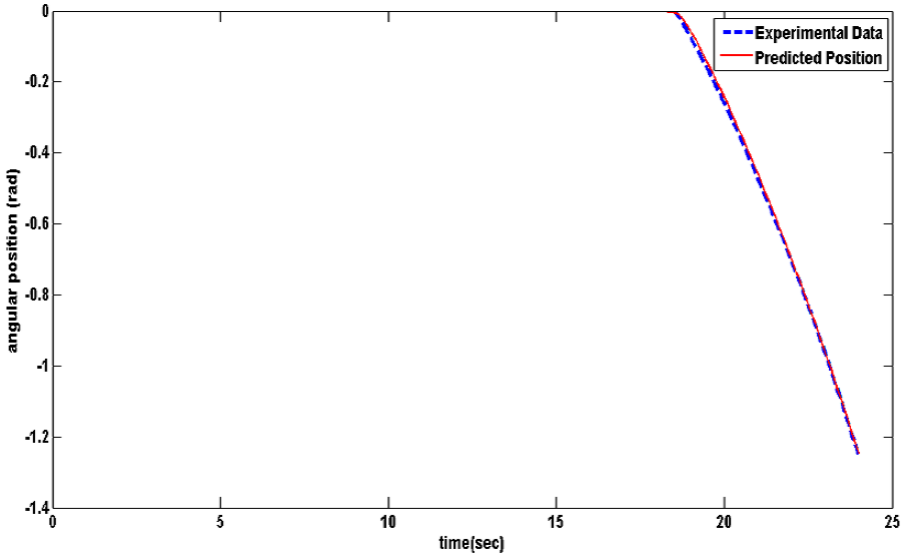

(a) Displacement plot

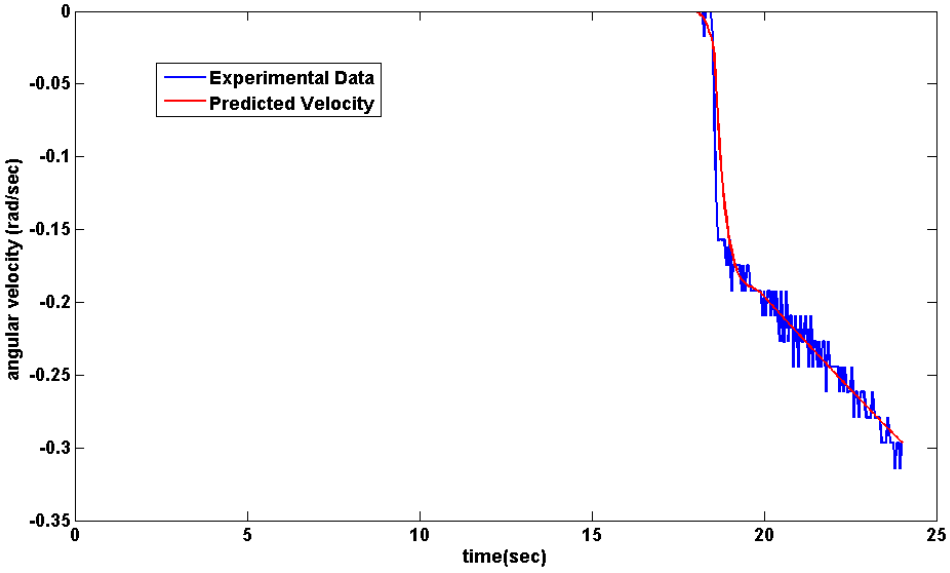

(b) Velocity plot

Figure 4.6: Curve fitting of Simulated and Experimental data

Chapter 5

Results

MBG models of PTP with various abstraction levels and fidelity are compared by respective equivalent models build by different methods. Ideal PTP model and PTP with payload model are compared with equivalent models in MSc ADAMS, a standard industry tool for modeling multi-body dynamic systems which uses Lagrangian formulation for system modeling. Bond Graph model of PTP's tilt mechanism is compared by models build in two commercial software; MATLAB and Pro Engineer. Bond Graph model of PTP's pan mechanism with mechanical imperfections is compared with experimental data. Simulation results and their comparisons are presented in the following text.

5.1 Ideal PTP

Configuration of the system under study should show non-linear behavior with appreciable coupling at high speeds. In order to simulate ideal PTP model, 20-sim is used. Parameters used in simulation are listed in Table 5.1.

Table 5.1: Simulation Parameters

Parameters	Value	Units
Pan_Jxx & Jzz	0.00053	$kg-m^2$
Pan_Jyy	0.00087	
Tilt_Jxx	0.00041	
Tilt_Jyy	0.00065	
Tilt_Jzz	0.00027	
Friction_pan & tilt	0.1	Kg-m/rad/s

In order to observe expected behavior, given input flows at pan and tilt revolute joints are quite high than what are practically desirable. Cubic type curve fitting is used

for transitioning flow amplitudes in motion profiles. Other details of motion profile of flow source are given in Table 5.2.

Table 5.2: Sources of flow parameters

Source of flow	Transition Time (sec)		Transition Amplitude (rad/s)	
	Start	End	Start	End
Tilt	0	0.5	0	10
Pan	2	2.5	0	10

Simulated results of MBG model from 20-sim is compared with its equivalent ADAMS model in Figure 5.1 and Figure 5.2. Results show good agreement with no significant difference.

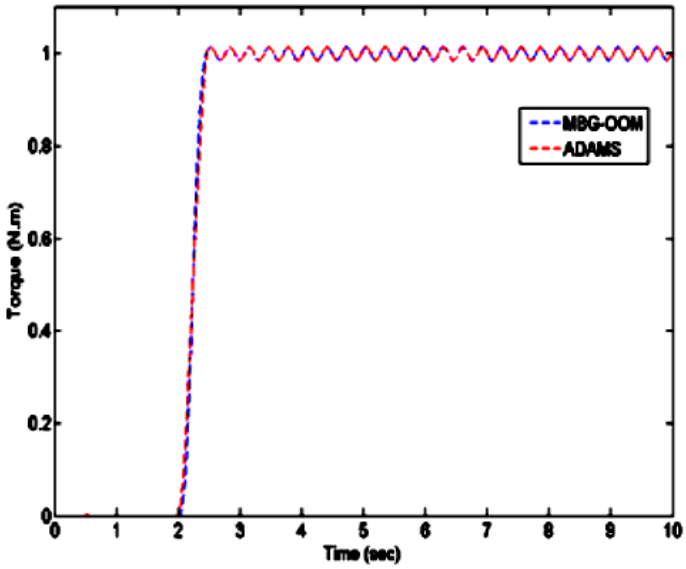

Figure 5.1: Comparison of Pan Torque from two models[8]

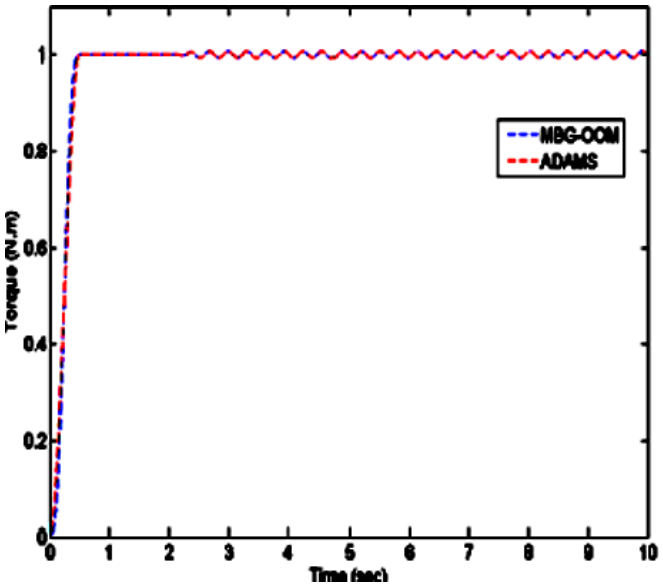

Figure 5.2: Comparison of Tilt Torque from two models[8]

Tilt and pan torques are plotted together in Figure 5.3 showing that coupling exist when both motion axes are actuated together. Use of high speed has pronounced this effect greatly, where this effect can be neglected while using practically desired speeds.

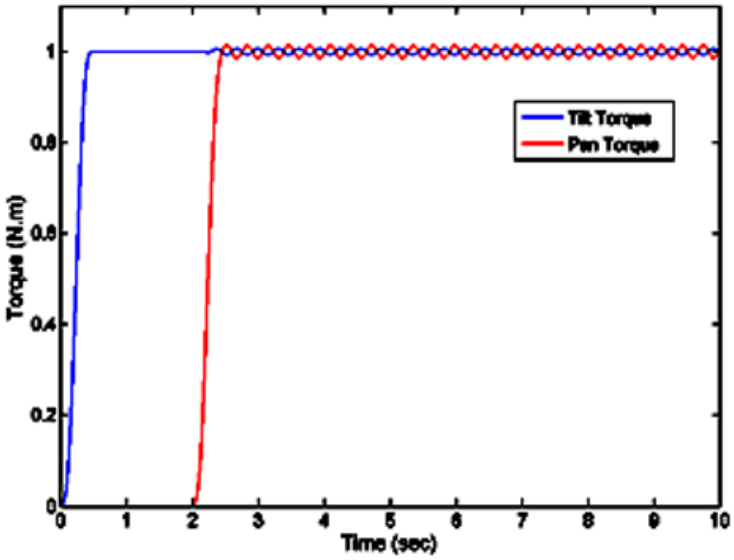

Figure 5.3: MBG-OOM model showing coupling[8]

5.2 PTP with Payload

The model is expected to show non-linear and coupled behavior. Pan torque during speed change should be dependent on the position in tilt mechanism. For simulating PTP-Payload model, PTP parameters are same as listed in Table 5.1; payload parameters are listed in Table 5.3.

Table 5.3: Payload Parameters

Parameters	Value	Units
Payload_mass	4.992	Kg
Payload_Jxx	0.0053	Kg-m2
Payload_Jyy & Jzz	0.0068	
Payload_cg_offset	0.01	m

Flow magnitudes used for simulating model are practically encountered in applications. Flow transition profile has cubic curve fitting. Other details of flow sources are given in Table 5.4.

Table 5.4: Flow sources parameters

Source of flow	Transition Time (sec)		Transition Amplitude (rad/s)	
	Start	End	Start	End
Tilt	0	0.5	0	0.5
Pan	2	2.5	0	1

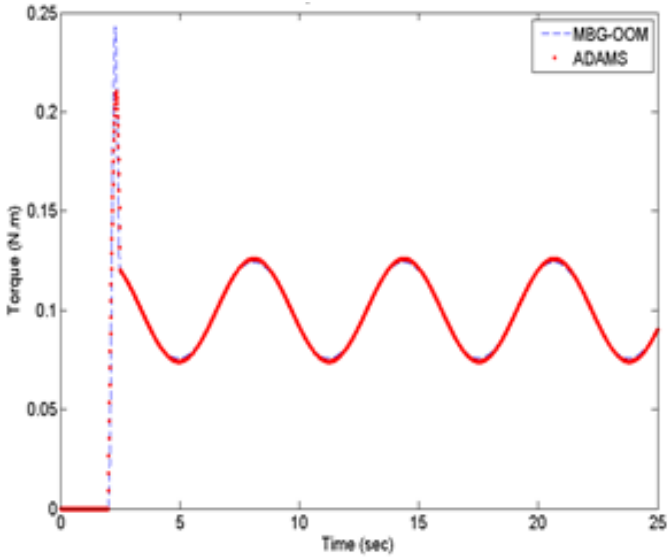

Figure 5.4: Comparison of pan torques from two models [8]

Comparison of pan and tilt torques computed from MBG-OOM and ADAMS model is shown in Figure 5.4 and Figure 5.5 respectively. Figure 5.4 shows slight deviation of required torque prediction during transition. MBG model predict slightly larger torque than ADAMS model. It is because of different slopes generated by build-in cubic fit motion profiles in 20-sim and ADAMS. During constant flow, torque prediction has negligible deviation.

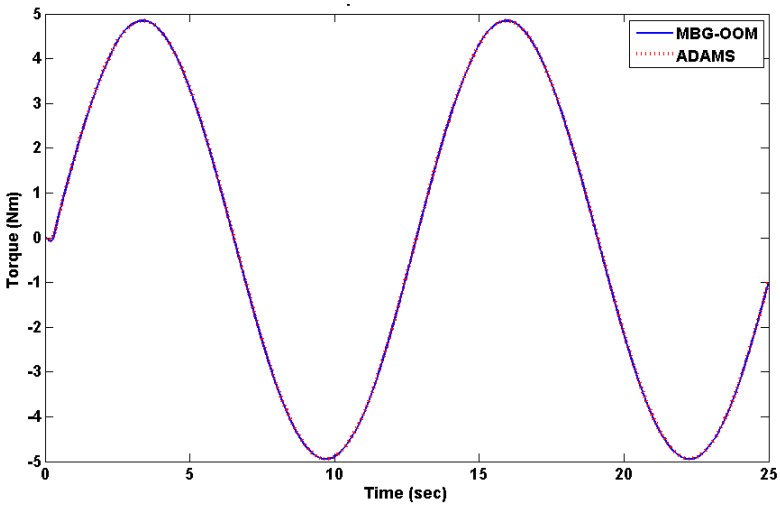

Figure 5.5: Comparison of tilt torques from two models

By comparing Figures 5.1, 5.2, 5.4 and 5.5, it can be seen that variance in pan and tilt torques in ideal PTP case is around 0.01Nm. It is around 0.025Nm in pan torque of PTP with payload, whereas tilt torque has a variance of around 5Nm. It can be inferred that coupling effects are not as largely pronounced in ideal PTP with partial mass symmetry

operated at high speeds than in PTP with payload even at much lower speeds. Similarly in PTP-Payload, it can be inferred that coupling effects actually appear in pan joint due to tilt motion, whereas in tilt axis coupling effects due to pan motion can be considered as negligible as compared to gravity effects. Appearance of gravity in tilt axis adds non-linearity in the tilt dynamics.

In order to show the coupling effects of tilt angle on the pan torque, another simulation is devised. Tilt angle is given an initial angle with no flows during simulation, while pan joint is given two cyclic pulses. The plots for required pan torque for different tilt angles are shown in Figure 5.6, showing that pan torque during speed transitions are dependent on the tilt angle due to coupling effects.

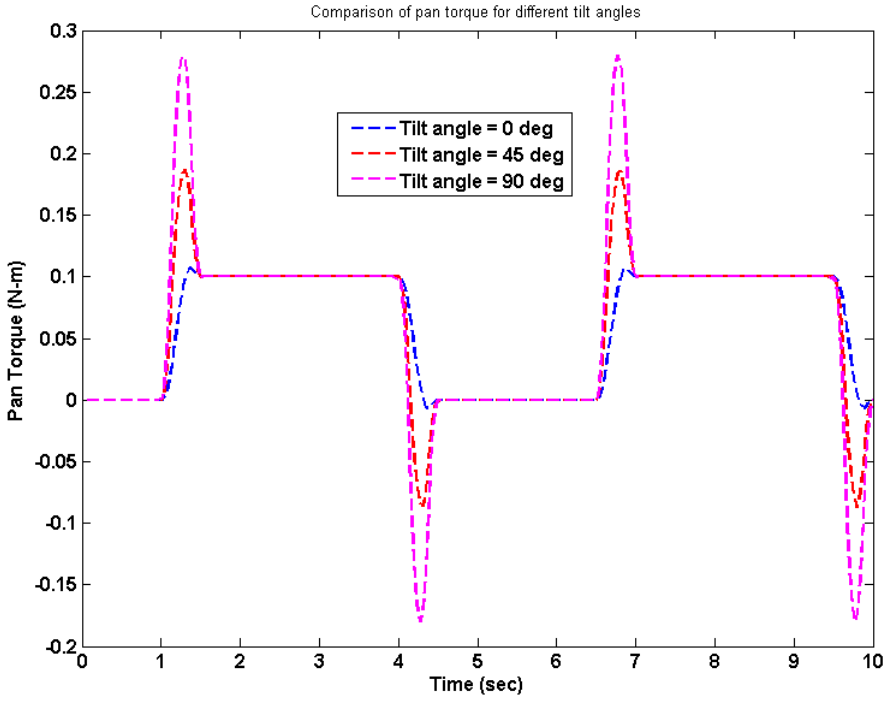

Figure 5.6: Required pan torque for different tilt angles[8]

5.3 PTP with Actuators

Results of pan actuation mechanism are discussed in next section with the pan friction and backlash model. In this section, results of Linear actuation and tilt mechanism are discussed.

BG model of tilt actuation mechanism is compared with an equivalent model, build using two different software packages; MATLAB's Simscape and Pro/Engineer. For

better understanding of how different models are utilized in results comparison, a flow chart is shown in Figure 5.7.

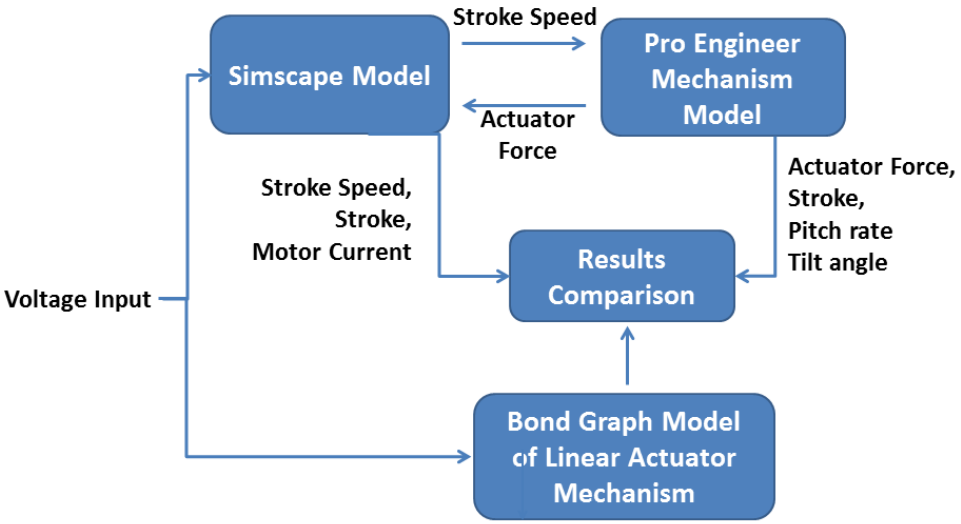

Figure 5.7: Data flow for tilt mechanism actuation comparison

MATLAB's Simscape model is used to capture the linear actuator dynamics. The model is build by using Simscape library for DC motor, Gear box and lead-screw. The model is equivalent to BG model of linear actuator shown in Figure 3.12. The Simscape model of linear actuator is shown in Figure 5.8.

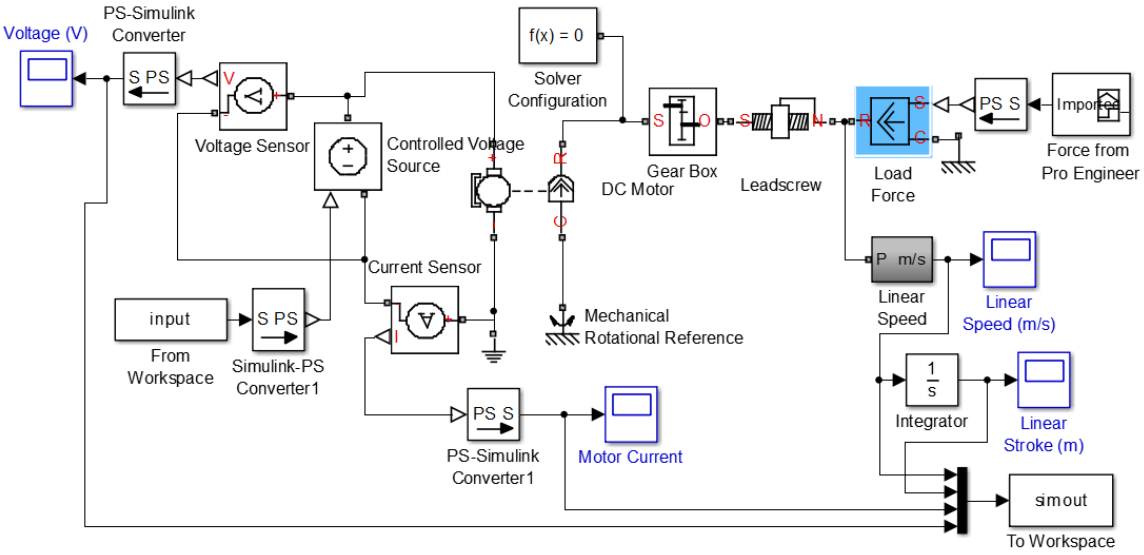

Figure 5.8: Simscape model of linear actuator

For comparing BG model for tilt mechanism comprising of mechanical linkage assembly, another model is created in Pro Engineer. Linear actuator stroke movement is

modeled as a slot joint. Stroke speed from Simscape's Linear actuator model is used as input velocity profile of linear servo motor placed at slot joint. Then Tilt angle, tilt angle rate and actuator force are computed and results are compared with BG model. Actuator force predicted by Pro Engineer model is fed again in Simscape Linear actuator model for estimating motor current. Important parameters used in simulation for DC geared motor are shown in Table 5.5, where Table 5.6 shows key parameters related to tilt mechanism.

Table 5.5: Linear actuator parameters used in simulation

Linear Actuator Parameters	Magnitude	Units
Motor inductance	0.00935	H
Motor resistance	17	Ω
Motor torque constant	0.044	Nm/A
Motor coil inertia	1.62e-6	kgm^2
Motor coil Viscous friction	1.1696e-4	Nm/(rad/s)
Gearing ratio	93	—
Lead Screw - lead	4	mm
Lead Screw - pitch diameter	8	mm
Lead-Screw - friction coefficient	0.15	—

Table 5.6: Tilt mechanism parameters

Tilt Mechanism Parameters	Magnitude	Units
Tilt mass	6.3785	kg
C.G offset	87.6228	mm
Joint Viscous Friction	10	Nm/(rad/s)
Principal Moment of Inertia (I_1, I_2, I_3)	$(3.8, 1.36, 3.89)x10^{-2}$	kgm^2
Initial Stroke	40.5022	mm
length of ground linkl_g	197.55	mm
min length of actuator,l_0	139	mm
length of connecting link, r	63.4133	mm
Initial Stroke	48.5	mm

The simulation results from Simscape with Pro Engineer are compared with bond graph model build in 20sim. The results are shown in Figures 5.9-5.14. The results show consistency without any major deviation.

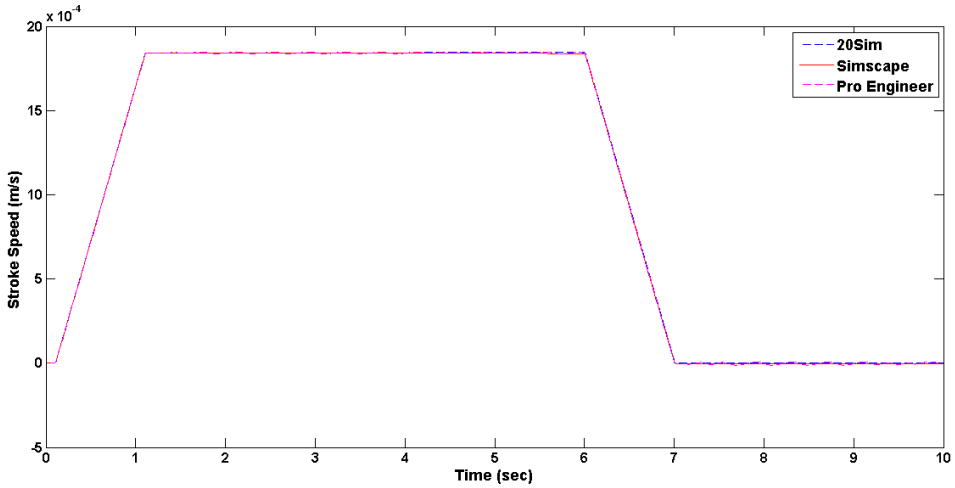

Figure 5.9: Linear actuator stroke speed

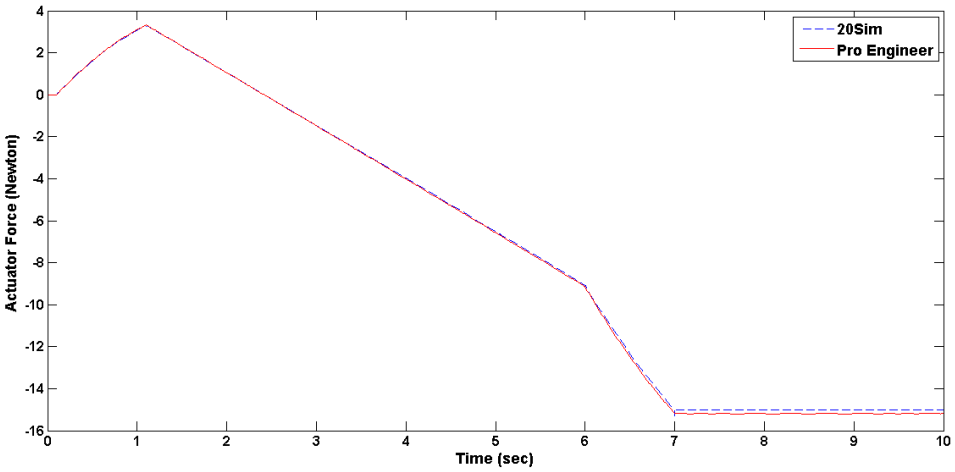

Figure 5.10: Actuator force

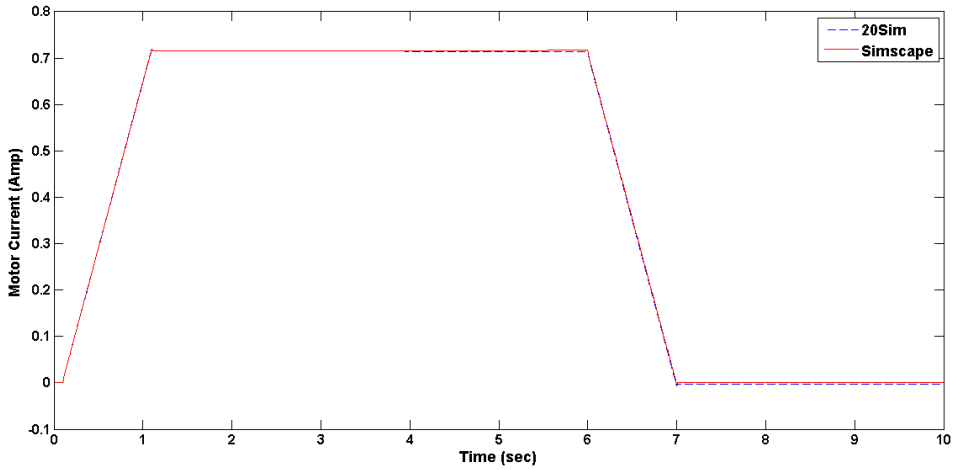

Figure 5.11: Motor current

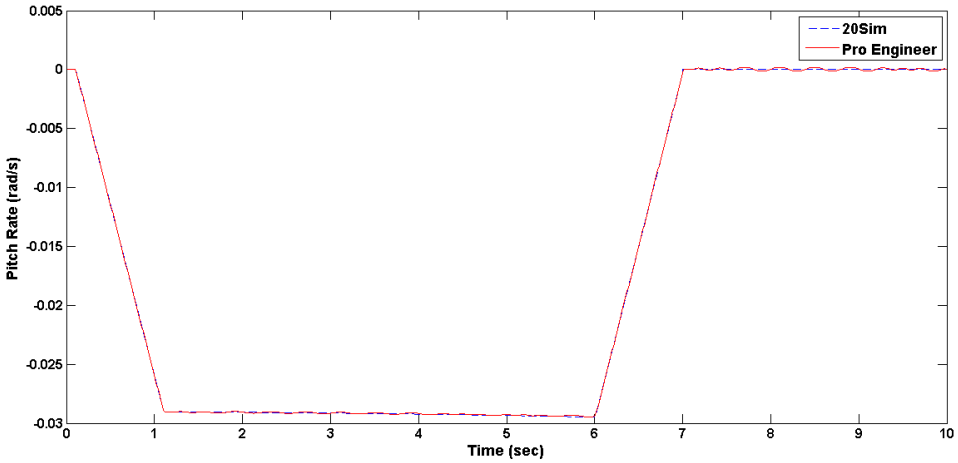

Figure 5.12: Pitch rate

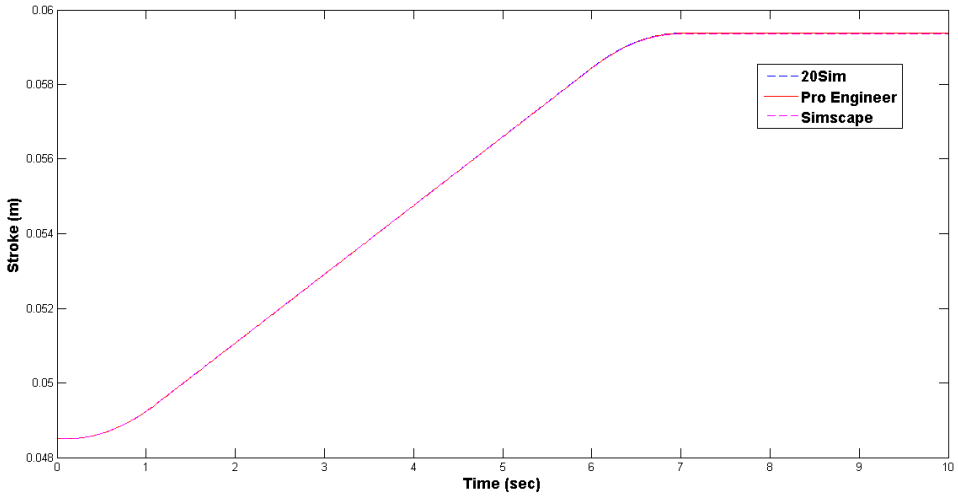

Figure 5.13: Stroke length

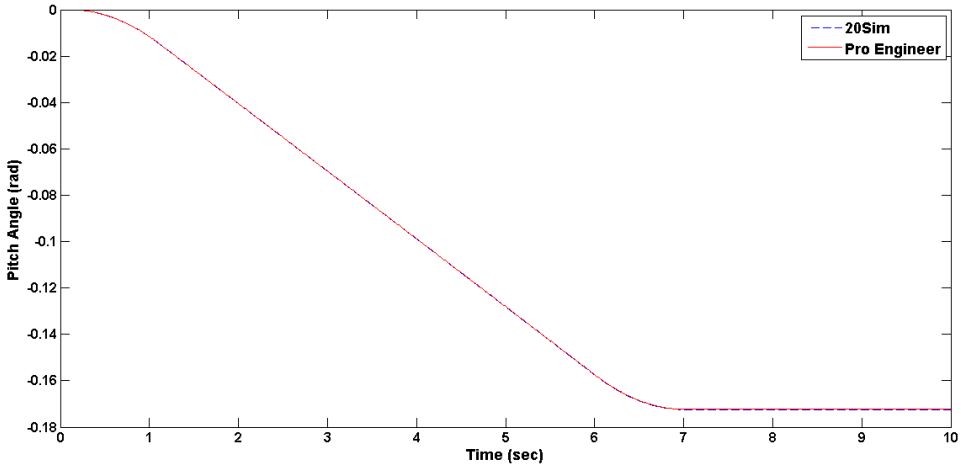

Figure 5.14: Tilt angle

In simulation, 24V is provided as trapezoidal input to the DC motor which results in outward motion of linear actuator. Tilt mechanism configuration is as such that the positive stroke of linear actuator causes negative tilt angle and tilt rates. Figure 5.10 clearly shows that initially actuator force is in positive/upward direction, in order to start motion in tilt axis. Later when body torque about tilt axis due to mass imbalance increases, actuator force gradually decreases and finally reverses its direction. This shows that actuator applies force to resist tilt body motion under gravity. Similarly, it can be observed that model predicts a non-zero actuator force in the end of simulation shows that actuator is applying a static force to counter body tilt torque even during non-operation mode when tilt angle has non-zero value. The effect of force direction reversal is enhanced for better visualization of system behavior in simulation by assuming relatively higher viscous coefficient at tilt joint.

5.4 PTP with pan friction and backlash

Mechanical imperfections of friction and backlash are only considered in pan joint modeling. The bond graph model of pan actuation mechanism with pan friction and backlash is compared with the experimental results. Key simulation parameters are shown in Table 5.7. Three different input profiles are used for comparison. All input profiles are given using PWM drive in open loop configuration. These input profiles includes step, ramp and trapezoidal voltage input. Results are presented one by one.

Table 5.7: Simulation parameters

Parameter	Magnitude	Unit
Motor Inductance	6.9e-3	H
Motor Resistance	12.9	Ω
Motor torque constant	0.0724	Nm/A
Motor Inertia	1.1e-5	Kgm^2
Gear ratio	500	—
Motor Friction (CSVS Friction Model)	Estimated parameters	
Backlash Gap	1.49	deg
shaft stiffness	5000	Nm/rad
Joint Viscous Friction	2	Nm/(rad/s)

5.4.1 Step Profile

Step input of 24Volts is given to the system in both directions. The input is given at 1.79 sec and kept at 24 Volt till 12 sec. Same input is given to 20sim model of PTP's pan actuation mechanism. The results in counter clock wise direction from the two sources are plotted in the Figure 5.15.

Table 5.8: Step input specifications

Test	Step Amplitudes(Volts)		Time(sec)	
	Minimum	Maximum	Start	End
1	0	24	1.79	12

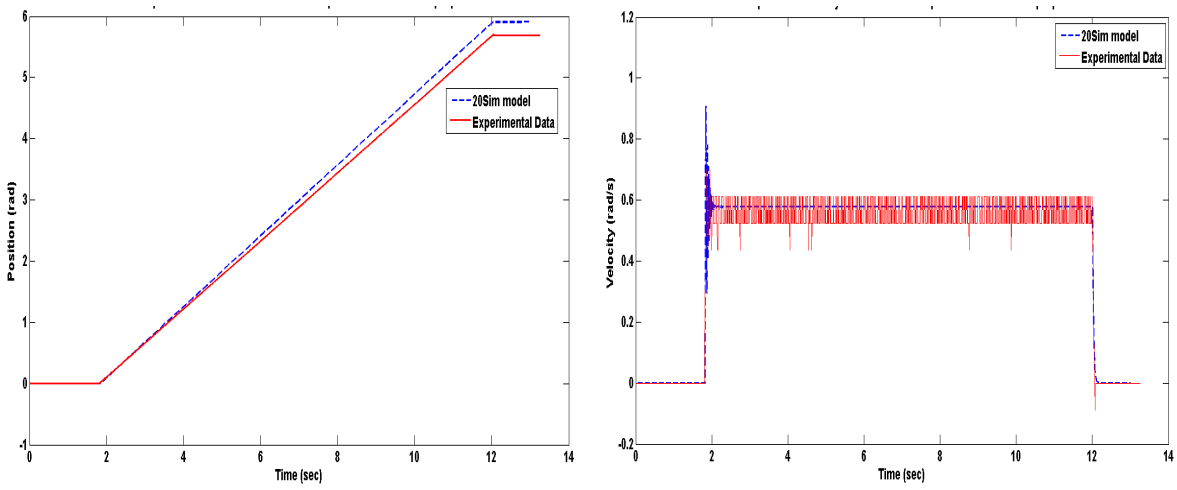

(a) Position

(b) Velocity

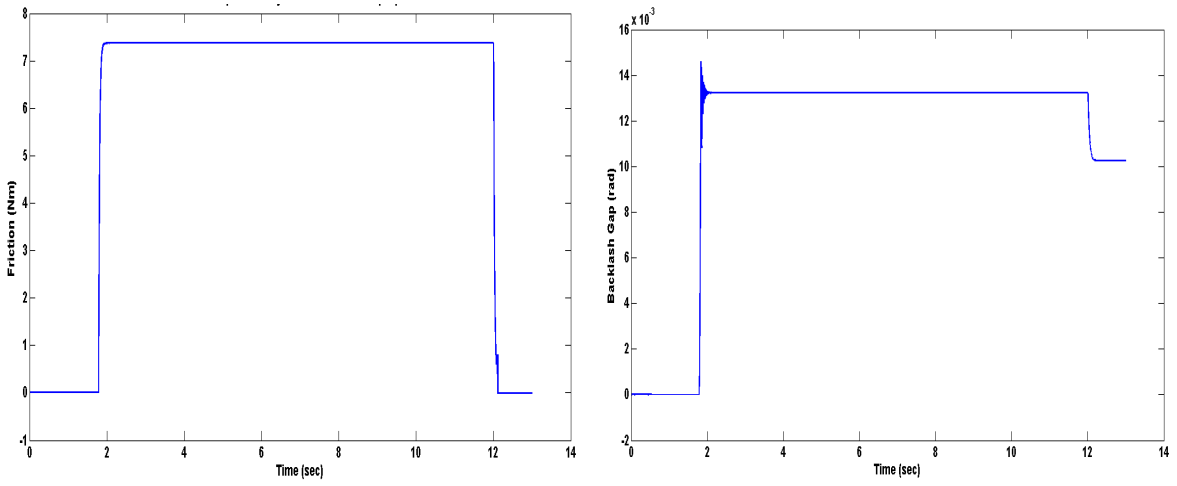

(c) Friction Estimated

(d) Backlash Gap

Figure 5.15: Results for step input 24 Volts

Simulation results are in agreement with experimental results. The L_2 norm of relative position error is found to be 0.0377 and 0.0378 while comparing results for 4.37

and 12.5 seconds respectively. L_2 norm is pretty consistent which shows that friction model is fairly good in predicting step input response. Oscillatory behavior is observed in experimental data before pan motion settles to steady state value. The behavior can be attributed to the elastic collision at the interface. 20sim model also captures similar oscillatory behavior. But this behavior doesn't represent elastic collision rather the behavior arises due to numerical simulation. Numerical solver switches system abruptly between contact and backlash mode before a stable contact mode is estimated. The effect can be adjusted by changing the viscous joint friction parameter.

5.4.2 Ramp Profile

Ramp input is given to the system with two different slopes. These have slopes of 48 Volts/sec and 2.4 Volts/sec. Details of these slopes are given in Table 5.9.

Table 5.9: Ramp inputs specifications

Test	Ramp Amplitudes(Volts)		Time(sec)		Slope (Volt/sec)
	Minimum	Maximum	Start	End	
1	0	24	0	0.5	48
2	0	24	0	10	2.4

Similarly these slopes were given to the 20sim model of PTP and results are compared. Figure 5.16 present results for ramp input with slope of 48 Volts/sec. The predicted position profile is pretty much the same as observed experimentally. L_2 norm of relative position error is found to be 0.0433 and 0.0365 for 0.51 and 0.88 seconds.

But for ramp input with slope 2.4 Volts/sec shown in Figure 5.17, it can be seen that the model's predicted position profile has greater deviation. L_2 norm of relative position error is found to be 0.2627 and 0.1065 for 5.12 and 10.57 seconds. The behavior suggest that the model predicts that the systems starts motion earlier than what is experimentally observed. The possible reason for the phenomenon is the variable breakaway torque which is considered as a function of rate of applied force. As rate of applied force decreases, this static friction tends to increase. Since friction model used cant predict any variance in breakaway torque therefore the model shows its limitation in predicting friction phenomenon accurately for slowly increasing torque.

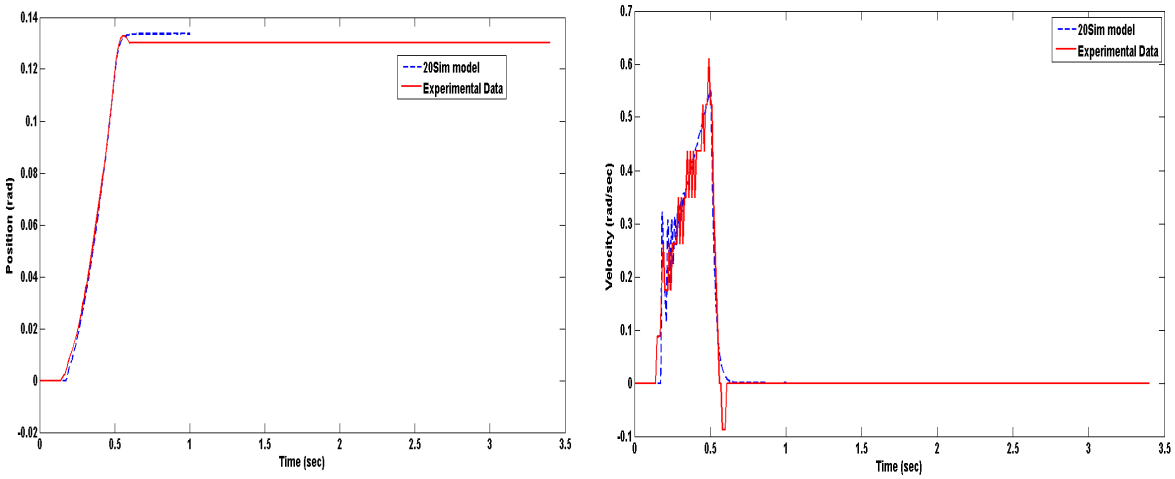

(a) Position

(b) Velocity

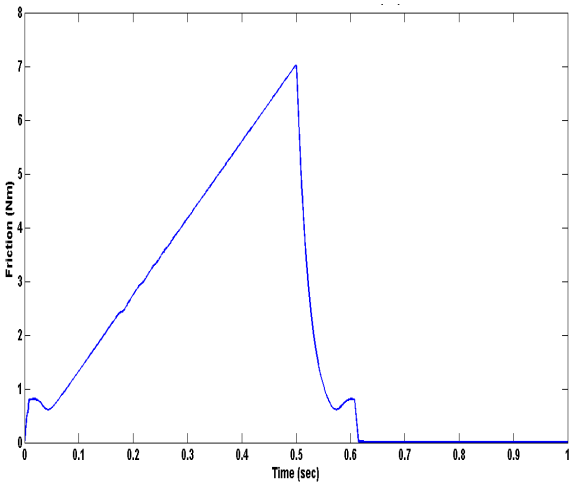

(c) Friction Estimated

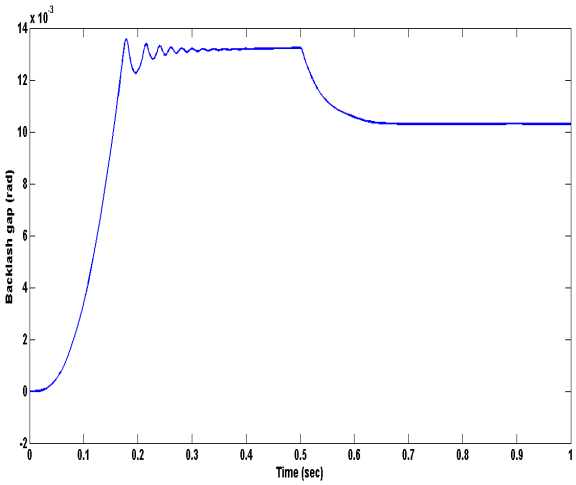

(d) Backlash Gap

Figure 5.16: Results for ramp input 48Volts/sec

Another phenomenon can be observed in Figure 5.16 which is not captured by the model. There exist a small peak in all the experimental data at the instance when ramp input is stopped and system input voltage is dropped to zero instantly. The phenomenon again suggests elastic collision during backlash impact. Since dead-zone model is used which assumes plastic deformation at the backlash impact, the model fails to capture the peak. The adjusted viscous friction is high enough this time and the behavior is not captured even by any numerical switching.

Moreover, it can be observed in all friction estimates that stribeck effect and distinct stick-slip regimes are observed. It can be seen that initially friction increases but there is no output motion. The system is in stiction mode. Then when the motion starts or system switches to slip mode, friction suddenly reduces showing stribeck effect. Later friction has a dominant linear viscous behavior.

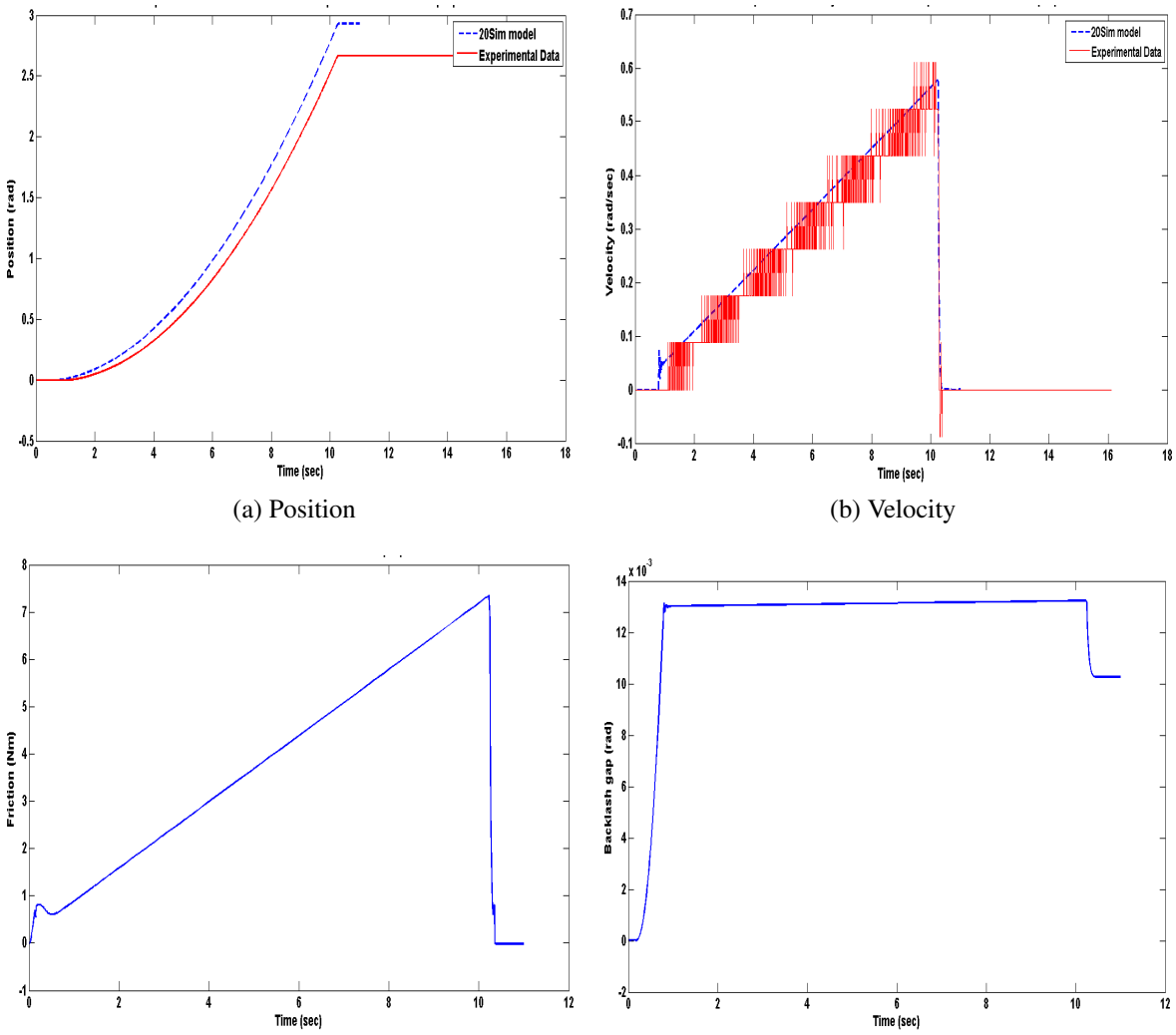

(a) Position

(b) Velocity

(c) Friction Estimated

(d) Backlash Gap

Figure 5.17: Results for ramp input 2.4 Volts/sec

5.4.3 Trapezoidal Profile

System is given a trapezoidal profile input which has ramp input for its first 0.5 sec then a steady 24V input for next 2.5 sec and then voltage is dropped using ramp profile to 0 volts in 0.5 seconds. Simulation results are plotted with experimental data in Figure 5.18. L_2 norm of relative position error is found to be 0.0305 and 0.035 for 2.63 and 4.28 seconds.

Experimental data show that there are no peaks or oscillatory behavior when input signal is returned to zero unlike it was observed in step and ramp input. The reason can be attributed that the rates of torque transfer in the run were not high enough to cause such behavior. The phenomenon could also be attributed to the limitation of sensing equipment. Figure 5.18c showing friction estimate, the stick-slip phenomenon

and stribeck effect is pronounced even during the ending of the input signal. The friction force suddenly increases in slip mode before system switches to stiction mode.

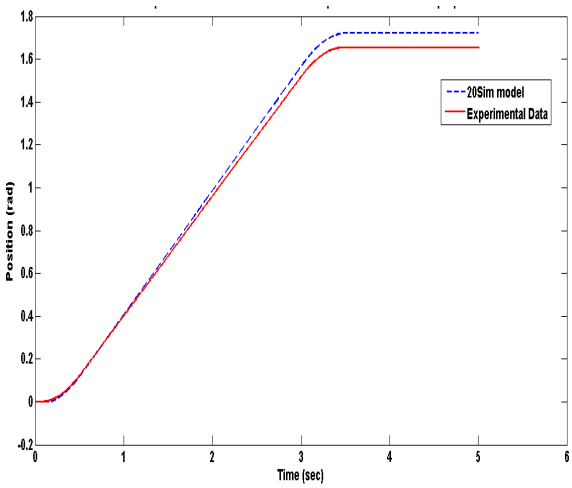

(a) Position

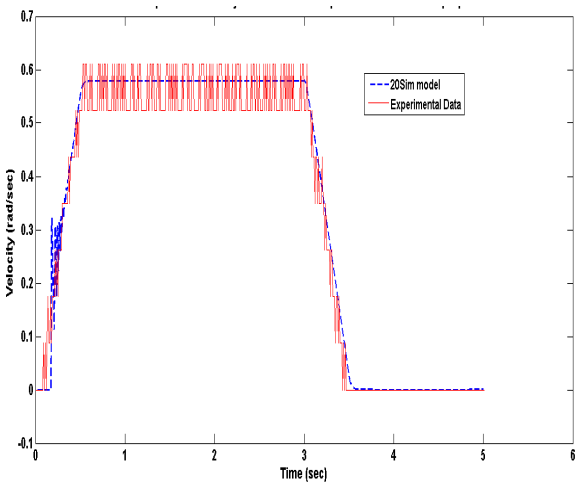

(b) Velocity

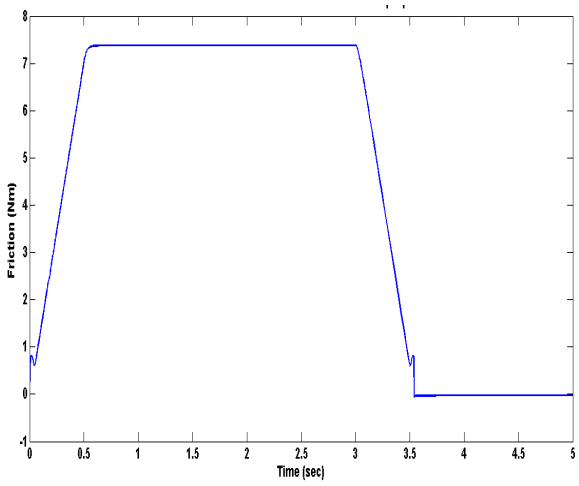

(c) Friction Estimated

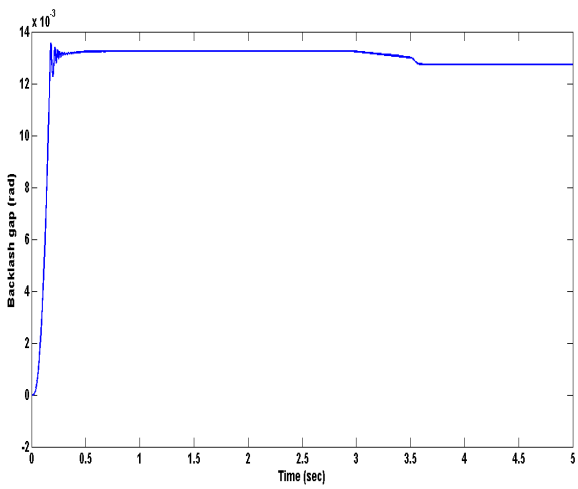

(d) Backlash Gap

Figure 5.18: Results for trapezoidal input

Chapter 6

Conclusion

The main goal of this research was to build a detailed model of Pan Tilt Platform with mechanical imperfections. The considered Pan Tilt Platform was that of NUST Ground Surveillance Radar. The study was conducted in modular way; i.e different PTP models were build in step wise manner; starting from basic or an ideal PTP system to more detailed models. Finally, PTP was modeled with actuation mechanism details of both pan and tilt axis along with mechanical imperfections of friction and backlash in pan joint.

6.1 Ideal PTP

PTP's dynamics was captured by Newton-Euler formulation using Object Oriented Modeling approach. The approach was used with multi-bond graph methodology to build an ideal PTP model. Multi-bond graph was used for its capability of handling multi-domain systems; while OOM approach helped in modeling system from its topology and kept modularity in the model. The study used 3D components library [13] and found that proposed library can be used to model multi-body systems. Later, MBG model of PTP was expanded to accommodate payload, thereby adding a mechanical imperfection of mass imbalance. PTP-payload model proved that system details can be added in modular approach with topological information using the combination of multi-bond graphs and OOM approach. MBG models were compared with equivalent models build in MSc ADAMS, an industry standard multi-body dynamics commercial package. The comparisons were primarily done to increase level of confidence for dif-

ferent transformations in the model. Results of both models were found in agreement.

6.2 Actuation modeling

In next step of detailed PTP model, actuation mechanisms were added in both pan and tilt joints. DC servomechanism was added as pan actuation mechanism whereas a linear actuator with mechanical linkages were used to model tilt mechanism details. DC servomechanism contained geared PMDC motor along with its controller loop. PMDC geared motor was modeled using scalar bond graphs whereas controller loop was modeled using iconic blocks in 20sim. Similarly, linear actuator and its mechanical linkages were modeled using scalar bond graphs. The bond graph model was compared with an equivalent model of assembly being built using two different software packages; MATLAB Simscape and Pro/Engineer. Linear actuator was modeled using standard component library in Simscape; whereas Pro Engineer was used to model the transformations in mechanical linkages. Comparison of tilt mechanism models show the utility of bond graphs for modeling of multi-domain systems.

6.3 Mechanical Imperfections

Final step of PTP detailing caters for mechanical imperfections of friction and backlash at pan joint. For the PTP case study at hand, tilt mechanism only required position control whereas pan mechanism required both position and velocity control. Considering practical utility, mechanical imperfections of friction and backlash are added in pan joint only.

Initially, it was planned to model friction using LuGre friction model but because of low resolution of sensing instrument than required to capture pre-sliding displacement, it was latter decided to use a general classic friction model of CSVS containing coulomb, static, viscous and stribeck friction parameters. These parameters were found from steady state friction-velocity map obtained from experimental data of Pan Tilt Platform of NUST Ground Surveillance Radar. MATLAB Optimization Toolbox was used for estimating required friction parameters. The classical friction model was found to capture the dynamics of system within the accepted range for step, fast ramp

and trapezoidal inputs. However, it showed limitations during slowly increasing torque ramp inputs where it possibly failed to predict variable breakaway torque phenomenon. Moreover, it was observed while estimation of inertia for pan body that there was appreciable difference between friction parameters that were estimated while using direct DC drive than PWM drive for the system. PWM drive appears to decrease the static and coulomb friction coefficients, thereby decreasing non-linearity of the friction. Viscous coefficient is more pronounced in PWM drive.

Similarly, backlash was modeled using deadzone model; a classical backlash model. The model assumed no internal damping in shafts and plastic collision during transition from backlash to contact mode. The model appears to work just fine by adding delays in input-output motion but clearly shows its limitation in capturing the observed phenomenon of elastic collision during mode transitions.

6.4 Future work

The build PTP model can be used in future for conducting model based control study of the system. It can not only be used to tune PID controller gains but can also be utilized for more complex controller designs. For capturing physical phenomenon involving friction and backlash with more accuracy, it is recommended that high resolution encoders along with standard data sampling equipment is used. More complicated mathematical models for friction and backlash can be incorporated in PTP model only if experimental setup can capture those phenomenon accurately.

Bibliography

[1] D. C. Karnopp, D. L. Margolis, and R. C. Rosenberg, *Modeling and Simulation of Mechatronic Systems*. John Wiley & Sons, Inc., fourth ed., 2006.

[2] P. Richard, M. Morarescu, and J. Buisson, "Bond graph modelling of hard nonlinearities in mechanics: A hybrid approach," *Nonlinear Analysis: Hybrid Systems*, vol. 2, pp. 922–951, Aug. 2008.

[3] R. T. M. Bride and F. E. Cellier, "A Bond-Graph Representation of a Two-Gimbal Gyroscope," in *International Conference on Bond Graph Modeling and Simulation*, no. 2, (Phoeniz, Arizona), 2001.

[4] M. Tiernego and J. Dixhoorn, "Three - Axis Platform Simulation : Bond Graph and Lagrangian Approach," *Journal of the Franklin Institute*, pp. 185–204, 1979.

[5] I. S. Sarwar, J. Iqbal, and A. M. Malik, "Modelling and motion control of a mechatronic system using BGM with intelligent controllers," *Simulation Modelling Practice and Theory*, vol. 18, pp. 1253–1265, Oct. 2010.

[6] D. Sheng, D. Fan, H. Luo, and X. Nie, "Bond Graph Approach to the Modeling and Simulation of a Two-Axis Pointing and Tracking System," in *2007 International Conference on Mechatronics and Automation*, pp. 2337–2341, Ieee, Aug. 2007.

[7] R. McBride and F. Cellier, "Object-Oriented Bond-Graph Modeling of a Gyroscopically Stabilized Camera Platform," *Simulation Series*, vol. 35, pp. 220–230, 2003.

[8] M. Haider, R. A. Azim, and W. U. H. Syed, "Multi-Bond Graph Modeling of Pan Tilt Platfom Using Object Oriented Modeling Approach," in *IASTED Third Asian*

Conference on Modeling, Identification and Control, no. AsiaMIC, pp. 112–119, 2013.

[9] M. Tiernego and A. Bos, "Modelling the Dynamics and Kinematics of Mechanical Systems with Multibond Graphs," *Journal of the Franklin Institute*, pp. 37–50, 1985.

[10] W. Borutzky, "Bond graph modeling from an object oriented modeling point of view," *Simulation Practice and Theory*, vol. 7, pp. 439–461, Dec. 1999.

[11] F. E. Cellier and D. Zimmer, "Wrapping Multi-Bond Graphs: A Structured Approach To Modeling Complex Multi-Body Dynamics," *ECMS 2006 Proceedings edited by: W. Borutzky, A. Orsoni, R. Zobel*, pp. 7–13, May 2006.

[12] C. Secchi, M. Bonfé, F. C, and B. R, "Object-Oriented Modeling of Complex Mechatronic Components for the Manufacturing Industry," *IEEE/ASME Transactions on Mechatronics*, vol. 12, no. 6, pp. 696–702, 2007.

[13] G. Filippini, D. Delarmelina, J. Pagano, J. P. Alianak, S. Junco, and N. Nigro, "Dynamics of multibody systems with bond graphs," *Mecanica computacional*, pp. 2943–2958, 2007.

[14] K. Worden, C. Wong, U. Parlitz, a. Hornstein, D. Engster, T. Tjahjowidodo, F. Al-Bender, D. Rizos, and S. Fassois, "Identification of pre-sliding and sliding friction dynamics: Grey box and black-box models," *Mechanical Systems and Signal Processing*, vol. 21, pp. 514–534, Jan. 2007.

[15] F. Altpeter, *Friction Modeling , Identification and Compensation*. PhD thesis, Swiss Federal Institute of Technology in Lausanne, 1999.

[16] C. Richard, *On the Identification and Haptic Display of Friction*. Phd thesis, Stanford University, 2000.

[17] R. Hensen, M. van de Molengraft, and M. Steinbuch, "Friction induced hunting limit cycles: A comparison between the LuGre and switch friction model," *Automatica*, vol. 39, pp. 2131–2137, Dec. 2003.

[18] J. A. D. Marchi, *Modeling of Dynamic Friction, Impact Backlash and Elastic Compliance nonlinearities in machine tools, with Applications to Asymmetric Viscous and Kinetic Friction Identification*. Phd thesis, Rensselaer Polytechnic Institute, 1998.

[19] B. Bona and M. Indri, "Friction Compensation in Robotics: an Overview," *Proceedings of the 44th IEEE Conference on Decision and Control*, vol. 2, pp. 4360–4367, 2005.

[20] L. Freidovich, A. Robertsson, A. Shiriaev, R. Johansson, and S. Member, "LuGre-Model-Based Friction Compensation," *IEEE Transactions on Control Systems Technology*, vol. 18, no. 1, pp. 194–200, 2010.

[21] C. C. D. Wit, H. Olsson, S. Member, K. J, and P. Lischinsky, "A New Model for Control of Systems with Friction," *IEEE Transactions on AUTOMATIC Control*, vol. 40, no. 3, pp. 419–425, 1995.

[22] V. V. Geffen, "A study of friction models and friction compensation," tech. rep., 2009.

[23] M. Hvoldal and C. Olesen, *Friction Modelling and Parameter Estimation for Hydraulic Asymmetrical Cylinders*. Master's thesis, Aalborg University, 2011.

[24] B. Armstrong-Helouvry, P. Dupont, and C. Canudas-de wit, "A Survey of Model, Analysis Tools and Compensation Methods for the Control of Machines with Friction," *Automatica*, vol. 30, no. 7, pp. 1083–1138, 1994.

[25] R. Waiboer, R. Aarts, and B. Jonker, "Velocity Dependence of Joint Friction in Robotic Manipulators with Gear Transmission," no. June, pp. 21–24, 2005.

[26] Y. Wang, Z. Xiong, H. Ding, and X. Zhu, "Nonlinear Friction Compensation and Disturbance Observer for a High-speed Motion Platform," in *Proceedings of the 2004 IEEE International Conference on Robotics and Automation*, pp. 4515–4520, 2004.

[27] M. Nordin and P.-O. Gutman, "Controlling mechanical systems with backlash - A survey," *Automatica*, vol. 38, pp. 1633–1649, Oct. 2002.

[28] R. V. Dwivedula and P. R. Pagilla, "Effect of Compliance and Backlash on the Output Speed of a Mechanical Transmission System," *Journal of Dynamic Systems, Measurement, and Control*, vol. 134, no. 3, p. 031010, 2012.

[29] M. Nordin, J. Galic', and P. Gutman, "New models for backlash and gear play," *International Journal of Adaptive Control and Signal Processing*, vol. 11, no. 1, pp. 49–63, 1997.

[30] L. Marton and B. Lantos, "Control of mechanical systems with Stribeck friction and backlash," *Systems & Control Letters*, vol. 58, pp. 141–147, Feb. 2009.

[31] T. Jukic and N. Peric, "Model based backlash compensation," *Proceedings of the 2001 American Control Conference. (Cat. No.01CH37148)*, vol. 2, pp. 775–780, 2001.

[32] J. Gerdes and V. Kumar, "An impact model of mechanical backlash for control system analysis," ... *Control Conference, 1995. Proceedings* ..., pp. 1–5, 1995.

[33] A. Mahindrakar and S. Kulkarni, "Bond Graph Analysis of the Engineering Systems using 20-Sim Software Tool," *International Journal of Engineering Science and Advanced Technology*, vol. 2, no. 5, pp. 1431–1434, 2012.

[34] M. Mellal, S. Adjerid, and D. Benazzouz, "Modeling and simulation of mechatronic system to integrated design of supervision: using a bond graph approach," in *25th European Conference on Modelling and Simulation*, 2011.

[35] H. Adibi-asl and G. Rideout, "Bond Graph Modeling and Simulation of a Full Car Model with Active Suspension," in *20th IASTED International Conference on Modelling and Simulation*, 2009.

[36] L. Silva and G. Magallan, "Modeling of electric vehicles dynamics with Multi-Bond Graphs," in *Vehicle Power and Propulsion Conference(VPPC)*, 2010.

[37] J. F. Broenink, "Introduction to Physical Systems Modelling with Bond Graphs." 1990.

[38] W. Borutzky, *Bond Graph Methodology - Development and Analysis of Multidisciplinary Dynamic System Models*. Springer London Dordrecht Heidelberg New York, 2010.

[39] H. Olsson and K. Å ström, "Friction models and friction compensation," *European Journal of Control*, vol. 4, pp. 176–195, 1998.

[40] K. J. Å ström and C. Canudas-de wit, "Revisting the LuGre Friction Model," *IEEE Control Systems Magazine*, no. December, pp. 101–114, 2008.

[41] C. Iurian, F. Ikhouane, and J. Rodellar, "Identification of a system with dry friction," tech. rep., 2005.

[42] Ultramotion, "Ultra Motion Bug Linear Actuator."

[43] R. McBride, *System analysis through bond graph modeling*. Phd thesis, The University of Arizona, 2005.

[44] C. C. de Wit and P. Lischinsky, "Adaptive Friction compensation with partially known dynamic friction model," *International Journal of Adaptive Control and Signal Processing*, vol. 11, pp. 65–80, 1997.

[45] T. Kumar and R. Banavar, "Identification of Friction in the 50/80 cm ARIES Schmidt Telescope Using the LuGre Model," in *18th IFAC World Congress*, pp. 980–985, 2011.

[46] The Mathworks Inc., "MATLAB Documentation," 2013.

[47] R. Kelly and J. Llamas, "Determination of viscous and coulomb friction by using velocity responses to torque ramp inputs," *International Conference on Robotics and Automation*, no. May, pp. 1740–1745, 1999.

Appendix

Appendix A: Backlash Experiment results

S.No	Measured Value
1	1.45
2	1.5
3	1.6
4	1.6
5	1.5
6	1.45
7	1.45
8	1.35
9	1.4
10	1.4
11	1.45
12	1.35
13	1.5
14	1.6
15	1.55
16	1.65
17	1.45
18	1.55
19	1.55
20	1.45
Average	1.49

Appendix B: MATLAB Code: Steady State Friction Parameters Estimation

dataimport;

```
%dataimport
clc clear all
%IMPORTFILE(FILETOREAD1) % Imports data from the specified file % FILETOREAD1: file to read
DELIMITER = '\t'; HEADERLINES = 1;
% Import the file Data = importdata('Joint friction parameters - selected data.txt', DELIMITER, HEADERLINES); %Data = importdata('omega-torque data.txt', DELIMITER, HEADERLINES); exp_data=Data.data;
w_positive = exp_data(:,1); Fss_positive = exp_data(:,2); w_negative = exp_data(:,3); Fss_negative = exp_data(:,4);
%%%%%%% for positive omega parameters%%%%%%%%%
xdata = w_positive; ydata = Fss_positive;
counter=1; iter = 0;
Tc = [0.53]; Ts = [0.6]; Ws = [0.01]; Tv = [14.36]; gamma = [2]
lb = [0.1 0.4 0.0001 1.999 10]; ub = [0.7 0.9 1 2.001 40];
for a = 1:length(Tc)
for b = 1:length(Ts)
for c = 1:length(Ws)
for d = 1:length(gamma)
for e = 1:length(Tv)
x0 = [Tc(a) Ts(b) Ws(c) gamma(d) Tv(e)];
iter = iter + 1
options = optimset('GradObj','on','MaxIter',2000,'TolX',1e-12,'MaxFunEvals',1000);
[x,ResidualVal] = lsqcurvefit(@steadyfriction,x0,xdata,ydata,lb,ub,options);
```

```
function F = steadyfriction(x,xdata)
F = (x(1) + (x(2)-x(1)) * exp (-1 * abs((xdata/x(3))).^x(4))) .*sign(xdata) + x(5)*xdata;
ResidualVal_array(:,counter)=ResidualVal;
x_array(:,counter) = x;
counter=counter+1;
end end end end end
Residual_backup=ResidualVal_array;
[minCost,Index] = min(ResidualVal_array)
Parameters_GlobalMin = x_array(:,Index)
for j = 1:counter
for i = 1:4
if sign(Parameters_GlobalMin(i,1)) == -1 || abs(Parameters_GlobalMin(i,1))
== 0
ResidualVal_array(1,Index) = 1e6;
[minCost,Index] = min(ResidualVal_array)
Parameters_GlobalMin = x_array(:,Index)
end end end
Parameter_positive_omega = Parameters_GlobalMin;
%%%%% for negative omega parameters %%%%%%%%%
xdata = w_negative;
ydata = Fss_negative;
counter=1;
iter = 0;
Tc = [0.65]; Ts = [0.82];
Ws = [0.02] Tv = [15.64];
gamma = [2] lb = [0.1 0.4 0.00001 1.999 10]; ub = [0.6 0.9 1 2.001 40];
for a = 1:length(Tc) for b = 1:length(Ts) for c = 1:length(Ws) for d =
1:length(gamma) for e = 1:length(Tv)
```

```
x0 = [Tc(a) Ts(b) Ws(c) gamma(d) Tv(e)]; iter = iter + 1
options = optimset('GradObj','on','MaxIter',3000,'TolX',1e-12,'MaxFunEvals',2000);
[x,ResidualVal] = lsqcurvefit(@steadyfriction,x0,xdata,ydata,lb,ub,options);
ResidualVal_array(:,counter)=ResidualVal;
x_array(:,counter) = x; counter=counter+1; end end end end end
Residual_backup=ResidualVal_array;
[minCost,Index] = min(ResidualVal_array)
Parameters_GlobalMin = x_array(:,Index)
for j = 1:counter for i = 1:4
if sign(Parameters_GlobalMin(i,1)) == -1 || abs(Parameters_GlobalMin(i,1))
== 0
ResidualVal_array(1,Index) = 1e6;
[minCost,Index] = min(ResidualVal_array)
Parameters_GlobalMin = x_array(:,Index) end end end
Parameter_negative_omega = Parameters_GlobalMin;
```

Appendix C: MATLAB Code: Parameters Estimation Using Ramp Input

```
clear all clc

data_reading;

nx = length(ydata);

Tc = [5]; Ts = [6.15]; Ws = [0.1]; Tv = [14];

for i = 1:length(J) for j = 1:length(Tc) for k = 1:length(Ts) for l = 1:length(Ws)
for m = 1:length(Tv)

x0 = [J(i) Tc(j) Ts(k) Ws(l) Tv(m)] ;

lb = [0.049 3 4 0.001 4]; ub = [0.051 10 10 1 12];

options = optimset('GradObj','on','MaxIter',3000,'TolX',1e-7,'MaxFunEvals',2000);

[x,ResidualVal,residual,exitflag] =

lsqcurvefit(@estimation_F_csvs,x0,xdata,ydata,lb,ub,options);

ResidualVal_array(:,counter)=ResidualVal; x_array(:,counter) = x;

counter=counter+1; end end end end end

datacomparison_F_csvs;

Residual_backup=ResidualVal_array; [minCost,Index] = min(ResidualVal_array)
Parameters_GlobalMin = x_array(:,Index);

for j = 1:counter for i = 1:3

if sign(Parameters_GlobalMin(i,1)) == -1

ResidualVal_array(1,Index)=1e6; [minCost,Index] = min(ResidualVal_array);

Parameters_GlobalMin = x_array(:,Index) end end end
```

```
function v_m = estimation_F_csvs(x,xdata)
y0 = [0 0];
options = odeset('RelTol',1e-4,'AbsTol',1e-4);
[t,y,ydot]=ode23tb(@system_equation_F_csvs,xdata,y0,options,x);

    function ydot = system_equation_F_csvs(t,y,x)
    Jm = 2.75; Js = x(1); Tc = x(2); Ts = x(3); Ws = x(4); Tv = x(5);
    ydot(1) = y(2);
    v = y(2); if abs(v) < 0.0000001 v = 0; end
    u = 0.0145*0.0724*500*(t);
    if abs(v) < 0.005 && abs(u)<Ts
    F = u;
    elseif abs(v) > 0.005
    F = ((Tc + (Ts - Tc)*exp(-1*abs((v/Ws))^2)))*sign(v) + Tv * v;
    elseif v == 0
    F= 0;
    else F = Ts * sign(u); end
    ydot(2) = (1/Jm+Js) * (u-F);
    ydot = [ydot(1);ydot(2)];

v_m = y(:,2);
```